Geomorphology 345 (2019) 106836

Contents lists available at ScienceDirect

Geomorphology

journal homepage: www.elsevier.com/locate/geomorph

A multi–methodological approach to reconstruct the configuration of a travertine fissure ridge system: The case of the Cukor quarry (Süttő, Gerecse Hills, Hungary)

Ágnes Török [a,b], Hannes Claes [b,c,*], Andrea Brogi [d,e], Domenico Liotta [d,e], Ádám Tóth [a], Andrea Mindszenty [a], István Kudó [f], Sándor Kele [g], Kate W. Huntington [h], Chuan–Chou Shen [i,j], Rudy Swennen [b]

[a] Institute of Geography and Earth Sciences, Department of Physical and Applied Geology, Eötvös Loránd University, Pázmány P. sétány 1/c, 1117 Budapest, Hungary
[b] Department of Earth and Environmental Sciences, KU Leuven, Celestijnenlaan 200E, 3001 Heverlee, Belgium
[c] Clay and Interface Mineralogy (CIM), Bunsenstrasse 8, RWTH Aachen University, 52072 Aachen, Germany
[d] Department of Earth and Geoenvironmental Sciences, University of Bari, Via Orabona, 4, 70125 Bari, Italy
[e] Institute of Geosciences and Earth Resources, IGG-CNR, Via Moruzzi 1, Pisa, Italy
[f] Robert Bosch Ltd., Gyömröi u. 104, 1103 Budapest, Hungary
[g] Institute for Geological and Geochemical Research, Research Centre for Astronomy and Earth Sciences, Hungarian Academy of Sciences, Budaörsi út 45, 1112 Budapest, Hungary
[h] Department of Earth and Space Sciences, University of Washington, Seattle, WA 98195, USA
[i] High–precision Mass Spectrometry and Environment Change Laboratory (HISPEC), Department of Geosciences, National Taiwan University, 10617 Taipei, Taiwan
[j] Research Centre for Future Earth, National Taiwan University, Taipei 10617, Taiwan

ARTICLE INFO

Article history:
Received 6 May 2019
Received in revised form 16 July 2019
Accepted 2 August 2019
Available online 06 August 2019

Keywords:
Continental carbonates
Neo–tectonics
Geophysics
Geochronology
Strontium isotopes
Clumped isotopes

ABSTRACT

Travertines are continental carbonates that precipitate from spring waters, mainly due to CO_2 degassing. They are widely quarried as building stone, which has led to numerous (often abandoned) travertine quarry outcrops. These and other outcrops, however, merely represent the surface expressions of the complex architecture of travertine bodies and their deep–rooted feeding systems. Integration of field observations and geochemical analyses with crucial subsurface geophysical data is required in order to fully understand travertine systems and their relationship to the local geological framework. Such a multi-methodological approach is illustrated here for the case of the abandoned Cukor quarry. Radio-magnetotelluric (RMT) and Electrical Resistivity Tomography (ERT) surveys provide unique insights into local tectonics, geobody architecture and the topography preceding travertine deposition. Altogether, the lens–shaped, isolated domal geobody with spring-proximal lithofacies and subvertical bedding, in addition to the contrasting geochemistry and age with surrounding travertine, enabled the unequivocal reconstruction of the dismantled Cukor fissure ridge. This study illustrates the high potential of this multi–methodological approach on poorly exposed, strongly weathered, quarried and tectonically deformed travertine bodies, and provides information on the complex feeding system beneath travertine deposits. Their reconstruction can be interpreted in light of the neo–tectonic expression of regional uplift, helps to complete the regional tectonic history and provides insights into older landscapes that lack preservation or would no longer be immediately recognized at the surface.

1. Introduction

Travertine (sensu stricto) deposits are spring-related continental carbonates forming, mainly due to CO_2 degassing, from calcium bicarbonate ($Ca(HCO_3)_2$) rich hydrothermal fluids (e.g. Capezzuoli et al., 2014). Calcareous tufa is their low-temperature equivalent, mainly forming from karstic waters with a higher microbiological influence (e.g. Pedley, 1990). Given the continuity between these endmembers, both of them are often grouped under the term travertine (sensu lato; Pentecost, 2005), as it is applied in this manuscript. High versus low degassing rates in association with predominantly abiogenic versus biogenic precipitation are the key factors determining the fabrics of travertine deposits (Pentecost, 2005). Travertine morphology is highly variable from aprons, fans and wedges, cascades and waterfalls, to mounds, pinnacles, cones and fissure ridges (e.g. Fig. 1; see also Della Porta, 2015). The morphology is controlled by topography, tectonic setting, substrate lithology, climate, vent location, discharge rates, flow paths and physico-chemical properties of the spring water (e.g. Chafetz and Folk, 1984; Altunel and Hancock, 1993a, 1993b; Pentecost, 2005; Della Porta, 2015; Mohammadi et al., 2019). During the past few decades, several studies have been published on travertine and its relation to ancient climate (e.g. Bertini et al., 2008) as well as to hydrothermal circulation and tectonic activity (e.g. Hancock

* Corresponding author at: Department of Earth and Environmental Sciences, KU Leuven, Celestijnenlaan 200E, 3001 Heverlee, Belgium.
E-mail address: hannes.claes@emr.rwth-aachen.de (H. Claes).

https://doi.org/10.1016/j.geomorph.2019.106836
0169-555X/

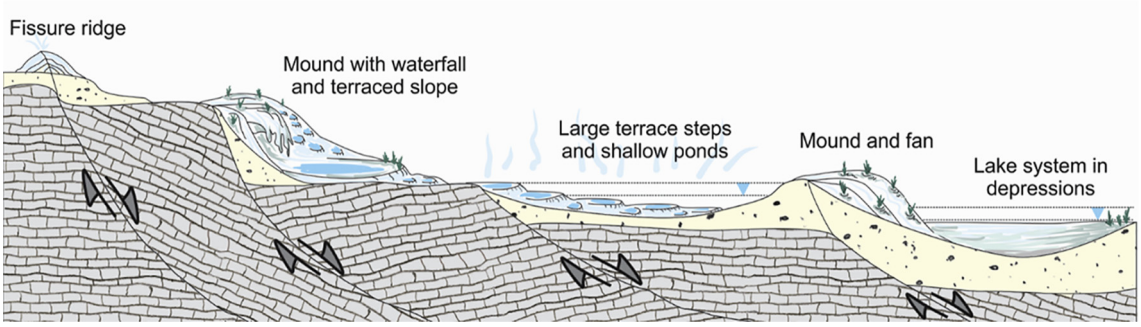

Fig. 1. Conceptual model of the main travertine morphologies. Note the relationship between the faults and the travertine bodies, in particular for the fissure ridge. For a more elaborate discussion on travertine morphologies see e.g. Della Porta (2015).

et al., 1999; Vignaroli et al., 2016; Berardi et al., 2016; Brogi et al., 2017). In addition, travertine deposits are studied because of their relevance to river terrace stratigraphy that allows incision/uplift rates to be inferred, e.g. in the Gerecse Hills along the Danube River (e.g. Kele, 2009; Ruszkiczay–Rüdiger et al., 2016; Ruszkiczay-Rüdiger et al., 2018). Furthermore, travertines potentially can be used as reservoir analogues for Brazilian Pre–Salt carbonate reservoirs (e.g. Ronchi and Cruciani, 2015; Soete et al., 2015; Claes et al., 2017).

In general, the spatial distribution of spring related travertine bodies, as unequivocal manifestations of feeding systems, is rather localized since most spring-type carbonate precipitations are restricted to spring orifices and their surroundings. Thermal spring locations are controlled by brittle structures channeling geothermal fluids from the deep reservoir up to the surface (Brogi et al., 2016a and references within). In fact, faults and related damage zones provide the most efficient pathways for fluid migration within the crust (i.e. Caine et al., 1996). Consequently, fault zones and related permeable rock volumes may result in a predictable pattern of travertine deposits (e.g. Curewitz and Karson, 1997; Hancock et al., 1999; Altunel and Karabacak, 2005; Brogi et al., 2014b). It implies, conversely, that their analysis provides information on recent tectonic activity and occurrence of deep geothermal systems (e.g. Minissale, 2004; Uysal et al., 2009; Van Noten et al., 2013; Brogi and Capezzuoli, 2014; Brogi et al., 2017).

The most prominent morpho–tectonic features related to spring-type travertine deposition are fissure ridges, representing carbonate deposits that readily precipitate along permeable fault zones (Bargar, 1978). Fissure ridges consist of elongated travertine masses with an apical fissure following the long axis of the body, and by two symmetrical or asymmetrical walls made up of bedded travertine, dipping away from the central fissure. The internal part of the fissure is often cut by a network of well–organized sealed fractures, almost parallel to the long axis of the fissure ridge, normally filled by laminated, syntaxial banded calcite/aragonite veins, almost parallel to the vein-walls and named as banded travertine (Altunel and Hancock, 1993a, 1993b). These veins, developed within the fault zone, have controlled the up-flow of the geothermal fluid upward (Altunel and Hancock, 1993a, 1993b; Mádl-Szőnyi and Tóth, 2015). Therefore, their analysis, in terms of geometry, age, evolution and geochemical properties, provides information about the structural features and timing of the fault system, and on the fluid path, from depth to surface (Hancock et al., 1999; Uysal et al., 2009; Frery et al., 2016; Capezzuoli et al., 2018). Fissure ridge travertine is characterized by distinct petrographic and geochemical features that preserved information on the depositing fluids and the ancient depositional conditions. As a consequence of fast precipitation, these spring-proximal deposits are often characterized by white, macroscopically crystalline texture that can form steep–sided geobodies (Pentecost, 2005). The shape of the fissure ridge body is a function of flow rate, precipitation rate and surface topography upon which deposition took place (Pentecost, 2005).

Enhanced erosion, induced by regional uplift, weathering and tectonic activity can, partly or completely, dismantle previously developed travertine bodies, complicating the reconstruction of their original architecture. In addition to this natural degradation, quarrying can further remove key features of a travertine body. In summary, the travertine can be eroded, dismantled and buried both by natural and anthropogenic processes. A further element of complexity is given by (early) diagenetic processes that, under highly saturated conditions, can lead to recrystallization (e.g. Török et al., 2017; De Boever et al., 2017). In these cases, an integrated approach is necessary to unravel the genesis of remaining travertine relicts. The classic approach that combines sedimentological, stratigraphic, structural and geochemical information does not suffice for strongly dismantled travertine bodies. In addition to the conventional techniques, well-targeted geophysical subsurface data provide the crucial information in reconstructing the original setting of the travertine morphotectonic features and in drawing conclusions about: (i) tectonic setting; (ii) fault geometry and kinematics; and (iii) the relationships between tectonic structures and geothermal fluid circulation at shallow crustal levels.

The Süttő travertine area in the Gerecse Hills of northern Hungary (Fig. 1) is a kilometer size, extensive travertine body of which the feeding system is unknown. The abandoned Cukor quarry represents a possible surface manifestation of a deeply rooted feeding system of the travertine complex. This study illustrates for the first time an integrated approach as a protocol to analyze dismantled travertine bodies, and in particular fissure ridge-type travertine deposits. Different kinds of decisive geophysical and geochemical surveys were introduced here in addition to the conventional techniques and proved their essential importance in the reconstruction of (i) the depositional setting, (ii) the antecedent topography of travertine deposition, (iii) the geometry and kinematics of the fault zone that promoted the hydrothermal fluid flow and travertine deposition, as well as (iv) the evolution of the travertine body before its dismantling, hereby helping to understand a tectonically-controlled feeding system and its contribution to the formation of an extensive travertine body.

2. Geological and geomorphological setting

The Süttő travertine complex is located in the Pannonian Basin, in the north–eastern corner of the Transdanubian Range (TR, Fig. 2), i.e. the Gerecse Hills. The Pannonian Basin is a Late Cenozoic structure surrounded by the Carpathian chain, which has developed since early-middle to late Miocene time as a result of extensional tectonics, involving thinning of the lithosphere (Royden and Horváth, 1988). This evolution gave rise to several sub–basins that offered the accommodation space for one to six kilometres thick late Miocene–Pliocene sediments, from marine, to lacustrine and, finally, to fluvial environments (Horváth and Cloetingh, 1996). The Transdanubian range is geologically an elongated synclinal structure and geomorphologically a series of slightly folded-imbricated and block-faulted horsts of southwest to northeast general strike (Pécsi, 1970). The Gerecse Hills, built up by Mesozoic successions (mainly dolostone, dolomitic limestone, limestone, marly–limestone and siliciclastic turbidites) and by Neogene–Quaternary sediments (only exposed in the eastern and southern parts) represent the north–easternmost part of the TR. These hills are

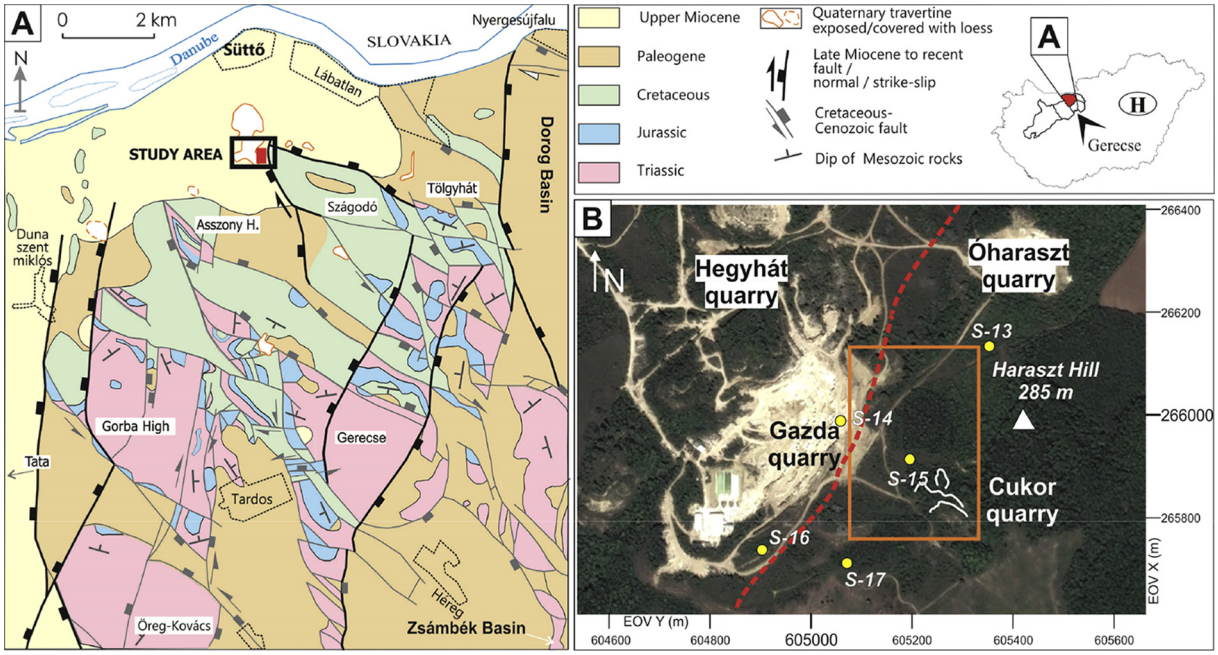

Fig. 2. (A) Geological sketch–map of the Gerecse Hills with Quaternary travertine occurrences (from Török et al., 2017). Black rectangle indicates the location of the map in Panel B while the orange rectangle shows the study area. (B) Satellite image of the Süttő travertine complex (modified after GoogleEarth.com). Yellow dots show the locations of the analyzed boreholes; white lines display the hidden travertine walls of the studied Cukor quarry outcrop. The red dashed line indicates the inferred NE–SW trending fault that controlled the paleo–spring location of the Gazda travertine body (Török et al., 2017). (*EOV is the Hungarian National Grid which is a transverse Mercator projection—positive X is pointed to North and positive Y is pointed to East. Coordinates are expressed in meters.*)

bordered, to the North by the Danube River valley, to the West by the Dunaalmás–Tata fault, to the South by the Zsámbék Basin, and to the East by the Dorog Basin (Fig. 2A).

The tectonic evolution of the Gerecse Hills is characterized by superimposed faulting events that took place since Mesozoic times (Bada et al., 1996; Fodor and Lantos, 1998; Fodor et al., 2018). In late Miocene time extension was associated with local transpressional settings in the Pannonian Basin. Some sectors, including the whole TR became uplifted (Horváth, 1993; Bada et al., 1996; Fodor et al., 1999) and partially eroded resulting in the exhumation of several fault-bounded basement units (Fig. 2A). Within the Gerecse Hills specifically, two main fault systems have been described (Fodor et al., 2013): a set of NW–SE trending Cretaceous to Cenozoic normal faults, and an array of NE–SW trending late Miocene to Present normal to strike– and oblique–slip faults (Fig. 2A).

Fault activity gave rise to local permeability conditions favoring the migration of hydrothermal fluids during the Pleistocene, with associated deposition of extensive travertine bodies (such as the Süttő travertine complex) along the river terraces of the Danube. To the south, in the Gerecse Hills, many of the travertine bodies were quarried since Roman times. Older travertine deposits formed on top of, or interfingering with, ancient river bedding deposits and thus at, or close to, the level of the Danube River (being the local base level of erosion; Pécsi, 1959; Scheuer and Schweitzer, 1988; Ruszkiczay–Rüdiger et al., 2016). However, due to uplift and induced erosion, these travertine deposits now occur at an altitude encompassing a range between 100 and 120 m above the level of the Danube River (Fig. 2B).

The studied Süttő area is located in a Danube River bend. The highest local point is formed by the Haraszt hill (285 m a.s.l.). Travertine formed in three geomorphological depositional environments along this hill: a) to the north of this hill on sub-horizontal plains which gently slope towards the N and NE, b) to the west of the hill in a steeply, to the SSW-sloping NS-elongated valley, and c) on the southern slope of the Haraszt hill (Török, 2018). Loess is draped over the morphological units subtly masking the landscape elements. Local mass flows and anthropogenic roads and quarrying further altered the landscape.

The Süttő travertine deposits have already been studied by several authors (e.g. Bakacsi and Mindszenty, 2004; Kele, 2009; Sierralta et al., 2010; Török et al., 2017). Based on their studies, we know that this travertine is mainly characterized by subhorizontal layers, predominantly deposited in lacustrine–palustrine environments. However, clear evidence for spring activity was never reported. The Cukor quarry is the smallest and most unique outcrop of the Süttő travertine area and might represent one of the feeding sources of travertine deposit. The Cukor spring-deposits are exposed in a 100 m long and 70 m wide abandoned quarry located on the southern slope of the Haraszt Hill (260–280 m a.s.l.) (Fig. 2). Ancient quarrying resulted in two ca. 3–5 m high working–levels, allowing observations of the inner structure of the travertine body. The travertine deposit is overlain by Quaternary loess, wind–blown sands and alluvial deposits, whereas the travertine substratum is represented by Paleogene-Neogene siliciclastic rocks (Csillag et al., 2018).

3. Methods

The investigation of travertine deposits requires a multi–methodological approach, especially with regard to neotectonic and paleoseismological studies (e.g. Brogi et al., 2014a, 2014b; Pola et al., 2014). The geometry of travertine bodies, their facies and spatial distribution, the location of the thermal springs, as well as the fault setting, in terms of geometry and kinematics, are fundamental data for the reconstruction of fossil depositional systems such as the Cukor travertine body. Faults can be buried and hidden due to subsequent deposition, displacements and/or erosion. Our research included: (1) detailed field mapping, coupled with structural and stratigraphic–sedimentological analyses, (2) petrographic analyses, (3) stable and clumped isotope measurements and (4) U-series dating, as well as, of crucial importance, (5) different kinds of geophysical surveys.

3.1. Fieldwork, data collection and petrographic analyses

Field mapping was carried out in an area of about 1 km^2 to reconstruct the relationships between the travertine deposit and its substratum, mainly made up of Miocene–Pliocene siliciclastic rocks and Pleistocene travertine and loess deposits (Novothny et al., 2011; Rolf et al., 2014). The description of the travertine lithotypes was carried

out by studying the quarry walls, cores, rock slabs, hand specimens and thin sections. The lithotypes can be related to the distance from the vent and thus help to spatially reconstruct the fissure ridge.

Data on the attitudes of the bedded travertine, as well as the strike and dip data of banded calcite veins and fractures were collected and compared with regional structures occurring in the surroundings. Opposing travertine bedding and the location and orientation of faults and fractures provide essential information with regard to the feeder system, the architecture of the fissure ridge and its tectonic control. Banded veins are typical for repetitive fluid flow events along the feeder fault. The assembly of these data helps to establish the relationship of the travertine to neotectonics structures. Representative samples were selected from each lithofacies spread over the entire outcrop in order to characterize: (a) the macro– and microfacies, focusing on the sedimentary rock constituents, which can provide information on the distance from the vent and local depositional conditions; (b) the porosity features; and (c) the diagenetic overprint. Samples for micro–petrography were resin–impregnated two times with a blue resin (3 samples) and with a fluorescent resin (21 samples), for optimal visualization of (micro-)porosity. Porosity not only can be linked to the local depositional environment, i.e. the lithotype, but also to the diagenetic overprint. In addition, potential microfractures can be better observed. The microscopic study was carried out with Leica DM LP and Olympus BH–2 microscopes. Cathodoluminescence (CL) microscopy provides information on potential (early) recrystallisation and other diagenetic processes. These are essential when evaluating samples for geochemistry. CL microscopy was executed on a Nikon Optiphot non–polarizing microscope with a modified Technosyn cathodoluminescence stage (model 8200 Mark II) and a Nikon Eclipse Ci–s polarizing microscope with CITL stage.

For petrographic description, Folk's (1959) and Dunham's (1962) classifications were used with the term phytohermal taken over from D'Argenio and Ferreri (1987). In addition, in order to describe pore types, the Choquette and Pray (1970) porosity classification was applied.

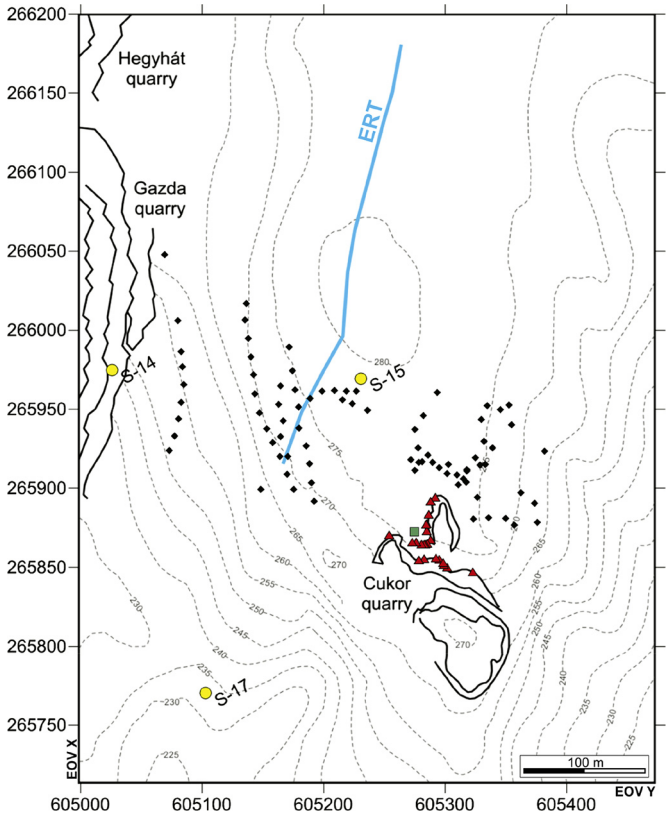

Fig. 3. Topographic map of the Cukor quarry and its surrounding (black lines – outcrop walls; black diamond – location of the radio magnetotelluric (RMT) measurements; blue line – section of the geoelectric profiling (ERT); yellow dots – location of the shallow boreholes; red triangles – location of stable O and C isotope samples; green rectangle – location of the clumped isotope sample).

3.2. Stable carbon-, oxygen-, strontium- and clumped isotopes

Thirty–one samples were micro–sampled from hand specimens for stable oxygen and carbon isotope analyses (Fig. 3). Care was taken to sample homogeneous parts of the samples in specific depositional or diagenetic fabrics. Fourteen samples were micro–drilled from the sparite phase and additionally, seventeen samples were taken from the micro–sparite phase of the studied samples. Along the veins, the geochemical signature most closely represents the feeder fluids before alteration by secondary processes. The other samples were selected spread over the outcrop to check vertical and lateral variation. The analyses were carried out at the Institute for Geological and Geochemical Research (Hungarian Academy of Sciences, Budapest, Hungary) using continuous flow technique with the H_3PO_4 digestion method (Spötl and Vennemann, 2003). The carbon and oxygen isotope ratios were determined in H_2 and CO_2 gases using a Finnigan Delta Plus XP continuous flow mass spectrometers equipped with an automated GasBench II. Duplicates of standards and samples were reproduced to be better than ±0.1‰, for both the oxygen and carbon isotopes. Systematic trends in stable isotopes can be related to vent proximity and provide information on processes like evaporation and degassing, or potential diagenetic resetting (Claes et al., 2019).

One massive, crystalline sample was taken from the Cukor quarry for clumped isotope measurements carried out at IsoLab (University of Washington, Seattle, WA, USA). Clumped isotopes can be used to determine the precipitation temperature and the stable oxygen isotope signature of the water. The latter subsequently can be used together with the stable isotope results of the travertine to calculate the estimated precipitation temperature of the other samples. In course of the measurement the procedures of Burgener et al. (2016), Schauer et al. (2016), and Kelson et al. (2017) were applied. The powder samples (2 aliquots of the sample, each 6–8 mg) were reacted in a common acid bath at 90 °C and cryogenically purified using an automated system. Purified CO_2 was analyzed using a multi-collector MAT253 IRMS (Thermo Scientific). The correction for ^{17}O interference used a value of 0.528 to relate abundances of ^{17}O and ^{18}O (Brand et al., 2010). Pressure baseline correction (He et al., 2012) was made by measuring the reference gas signal 0.0084 V down voltage of the mass 46 peak center. Samples were converted to the absolute Δ_{47} reference frame (Dennis et al., 2011). Temperatures were calculated from measured Δ_{47} values using the calibration of Kelson et al. (2017), which was generated in the same laboratory as our sample data. In the course of the Δ_{47} measurement stable oxygen and carbon isotopic values of the samples were also measured which help to check for consistency.

For determination of the rocks which presumably acted as carbonate sources for the travertine precipitating fluids and for verification of the geochemical relationship between the Cukor travertine deposits and the other travertine outcrops of the Süttő travertine, radiogenic strontium isotope measurements were also carried out on 15 samples. The samples were chosen to cover the whole Süttő area (different quarries), independent of the lithofacies/lithotype since these should not influence the signature. Care was taken to sample homogeneous pristine, i.e. not weathered, samples. The powder samples were analyzed at the "Université Libre de Bruxelles" (Belgium) following the procedure of Snoeck et al. (2015). The samples were pre-treated by a 3-minute long immersion in a 1 M acid bath and ultrasonication, followed by three rinsing cycles of 10 min with MiliQ water. Sub-boiled concentrated nitric acid (at 120 °C) was used for subsequent acid digestion. Afterwards, samples were purified using chromatography on ion-exchange resins (Snoeck et al., 2015). Isotopic ratios were acquired

using a Nu Plasma MC-ICP mass spectrometer. Raw data were corrected based on the standard-sample bracketing method of Weis et al. (2006). The analytical precision (1σ) is estimated below ±0.03. Data visualization via box plots follows the philosophy of Krzywinski and Almtan (2014).

3.3. U–Th dating

Four, 50 to 100 mg travertine samples were dated with U-Th techniques at the High–Precision Mass Spectrometry and Environmental Change Laboratory (HISPEC), Department of Geosciences, (National Taiwan University, Taipei, Taiwan). Three samples were selected from the bedded travertine and one from the banded travertine layer from the middle part of the travertine body. Care was taken to select samples with absence of alteration. In addition, the selected samples were massive, clean, and crystalline in order to avoid influence of detrital material or recrystallisation. A triple–spike, 229Th–233U–236U, isotope dilution method (Shen et al., 2002) was used to determine/U-Th isotopic and concentration data. Instrumental analyses were carried out on a multi–collector inductively coupled plasma mass spectrometer (MC–ICP–MS), Thermo Electron Neptune (Shen et al., 2012). Uncertainties in the U-Th isotopic data were calculated offline (Shen et al., 2002) at the 2σ level and include corrections for blanks, multiplier dark noise, abundance sensitivity, and contents of the four nuclides in spike solution. Half-lives of U-Th nuclides used for age calculation after Cheng et al. (2013).

3.4. Radiomagnetotelluric survey (RMT) and geoelectric profiling (ERT)

The radiomagnetotelluric survey (RMT) was carried out with equipment constructed by the Centre for Hydrogeology and Geothermics (CHYN) of Neuchâtel, Switzerland (Turberg et al., 1994; Bosch, 2002), allowing to detect different electrostratigraphic units (EsU). The latter correspond to relatively homogeneous layers, defined based on resistivity contrasts (Mele et al., 2012; Bersezio et al., 2012). This implies that intact travertine would belong to one EsU, while fractured travertine and other lithologies would belong to other EsUs. Altogether 83 RMT measurements were performed covering the outcropping travertine of the Cukor quarry and the eastern corner of the Gazda quarry as well as the area in between (Fig. 3) in order to map the lateral and vertical extension of the travertine body in the subsurface, but also the confining layers. RMT is a suitable tool to reconstruct the antecedent topography and its relationship to the fault network. The direction of the three applied antennas was N120–130° and their frequencies were 234 kHz (Beidweiler, Luxembourg), 77.5 kHz (Mainflingen, Germany) and 24 kHz (Cutler, Maine, USA). FITVLF2 inversion software was used for processing quantitative data (Fischer et al., 1981) and to calculate the actual resistivity and thickness of the units. Resistivity and topographic maps were prepared with software Surfer using the local polynomial interpolation method.

A 280 m long geoelectric profile was measured by GEOMEGA (Geological Exploration and Environmental Services Ltd) in dipole–dipole array (Fig. 3) to investigate the travertine connection between Gazda and Cukor quarries and to map tectonic structures. Spacing between the electrodes was 4 m and the average penetration depth was 50–60 m. The resistivity profile was measured with an ARES–G Automatic Resistivity system. Apparent resistivities were transformed into pseudo cross–sections with RES2Dinv® software to represent the terrain electric resistivity distribution.

The aim of the geophysical approach is to verify the extent of the travertine underneath the sedimentary cover and to highlight possible mechanical discontinuities, marked by sudden changes in the measured values (Török, 2018).

4. Data analysis

The data from field observations, micro–petrographic studies, stable oxygen-, carbon isotopic-, strontium ($^{87}Sr/^{86}Sr$), clumped (Δ_{47}) analyses, and U-series dating as well as geophysical surveys provide information on the: (1) fault network and travertine deposit; (2) depositional conditions and early–diagenetic processes; (3) antecedent topography and its relationship to the fault system controlling the pathway of the hydrothermal fluids producing the travertine deposit; and (4) age of the travertine deposit.

4.1. Travertine deposit of the Cukor quarry

The Cukor quarry (Fig. 2B) consists of two main abandoned excavations located at different levels with an approximate size of 100 by 70 m (Fig. 4A). The maximum height of the fresh–cut walls reaches 20 m. Travertine beds (0.5–1 m thick), exposed in both levels, are steeply dipping up to sub–vertical, in contrast with the general sub–horizontal dipping attitude of the travertine beds characterizing the rest of the Süttő travertine (Török et al., 2017). The bedding attitudes indicate two opposite dipping directions (Fig. 4A): travertine beds, occurring in the NE part of the quarry are steeply dipping towards the NE, with angles of 63° (±9.5°) and a strike of N142° (±11), while in the SW part of the outcrop they are characterized by 53° (±20) SW dipping beds, and strike N102° (±9°). Beds are dipping away from a central zone having NW–SE strike. The northern beds in the NE part of the quarry are steeper with respect to those cropping out in the southern part. The central zone of the travertine body is cut by NW–SE trending banded calcite veins, which are poorly preserved. NE–SW trending fractures have also been observed (Fig. 4A). These are filled by the overlying loess and do not show any apparent off-set (Fig. 4B–D). In the walls of each fracture, banded calcite veins are also present composed of reddish and blackish colored calcite bands (Fig. 4B–D), suggesting that fractures acted as conduits for hydrothermal fluids. These fractures were filled up by loess subsequently, during their later development.

The travertine body consists of five sedimentary lithofacies characterized by sugar–like texture (i.e. white, crystalline appearance). Spatial distribution and their macroscopic characteristics are illustrated in Figs. 4 and 5 and described below.

Massive crystalline travertine consists of macroscopically white, crystalline calcite (Fig. 5A). Randomly distributed small (0.5 to 1 cm in size) irregular pores, coated bubbles and molds of reworked phytoclasts are characteristic for this lithofacies (Fig. 5B). The massive crystalline travertine lithofacies forms 1–3 m thick, sub–vertical beds (Fig. 5I) that are dipping towards the NE within the upper excavation level, whereas SW gently dipping beds can be observed within the lower level of the quarry. The massive crystalline travertine lithofacies has been recognized over the entire outcrop where no interfingering with other lithofacies has been observed.

Phytohermal crystalline travertine is made up of massive, white crystalline travertine, possessing a dense network of in situ straw–like phytomolds (Fig. 5C). The highly irregular pore network is partially filled with calcite cement, however, it is locally enlarged slightly by karstification. The size of the vertically oriented phytomoldic pores ranges between 1 and 10 cm. The phytohermal travertine lithofacies consists of 0.5 to 1 m thick beds, that are oriented parallel to those of the massive crystalline travertine lithofacies, with which they alternate. Dip angles slightly decrease from the middle part towards the northern and southern edges of the outcrop.

Thin–bedded/laminated crystalline travertine is characterized by 0.5–2 cm thin crystalline layers (Fig. 5D). Each layer is separated from its neighbors by layer parallel elongated pores, partly filled by calcite cement. The diameter of these pseudo–fenestral pores ranges between 3 and 7 cm. Some smaller – 3 to 5 mm in diameter – isolated irregular pores can also be observed within the individual laminae. Locally, a black manganese oxi/hydroxide zone was observed within the pore–filling calcite with a characteristic thickness of 1 to 2 cm. The slightly wavy laminae form 50 to 70 cm thick beds that occur in both outcrop levels (Fig. 5D). The laminated packages are interbedded with massive and phytohermal travertine lithofacies displaying a similar geometrical setting as the enclosing travertines.

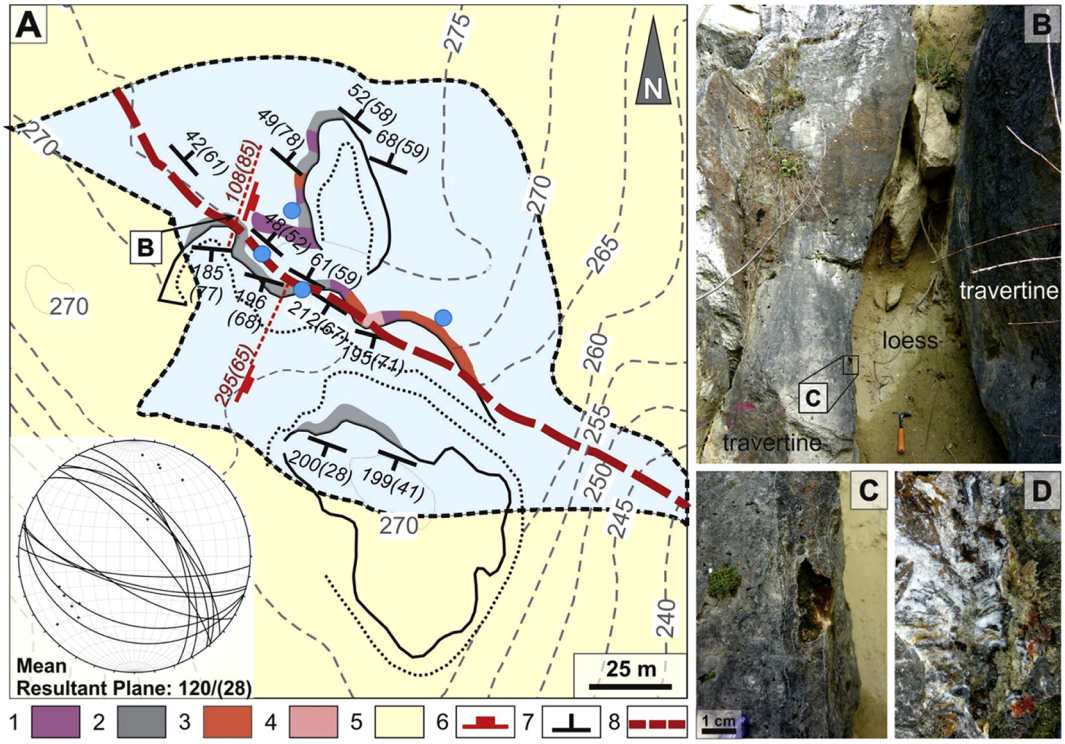

Fig. 4. (A) Sketch–map of the Cukor quarry showing the different lithofacies and their dipping attitudes. Stereographic projection indicates the dip of the travertine beds. (B) Loess filling the NE–SW trending fissure. Its location is indicated in Panel A. (C, D) Black and reddish banded calcite forming the vertical veins. Legend: 1: massive crystalline travertine; 2: phytohermal travertine; 3: lithoclastic (breccia) travertine; 4: micro terraces; 5: stratal dip; 6: fracture dip, 7: supposed NW–SE oriented normal fault based on field observations; blue dots represent the sample locations of U–series dating, black dashed line shows the boundary between the travertine outcrop and the covering loess and the light blue patch bordered by black dashed line represents the exposed area of the travertine body.

Micro terraces are built up of 1 to 3 cm thick, white massive layers that are separated by slightly wavy porous horizons (Fig. 5E). Along these surfaces vertically elongated pores – a few mm in length – are lined up acting as joint surfaces. Micro terraces (Fig. 5F) are made up of a few mm high micro–dams that are separated by shallow – <3–5 mm deep – micro-pools. The distance between the individual micro–dams ranges from 0.5 to 2 cm (Fig. 5F). This lithofacies appears in the middle of the lower quarry level forming a slightly wavy, 1.5 m thick layer that is traceable laterally over a distance of up to 5 m. The layers of micro terraces are displaced by several small fractures with a vertical displacement of ca. 20–35 cm. The general dip of the layer is 40° to the SW, however, it locally changes due to the displacements. This lithofacies is surrounded by lithoclastic (breccia) lithofacies.

Lithoclastic (breccia) travertine consists of reworked travertine and calcite clasts (Fig. 5G, H). The size of the angular clasts ranges from 0.5 to 10 cm in diameter. Clasts are embedded in weakly consolidated orange colored carbonate mud, hereby forming a matrix-supported structure. Locally, thin calcite encrustation was observed around groups of lithoclasts (Fig. 5H). It consists of 1 to 3 cm thick crusts containing a thin (few mm) black manganese oxy/hydroxide rim. Lithoclastic travertine lithofacies is exposed in the lower part of the Cukor quarry. Due to the ancient mining activity, and to the dense vegetation, this lithofacies can only be traced in the central part of the quarry up to its eastern edge. Neither bedding (including lateral and vertical variations) nor any other structure can be observed within this lithofacies. The contact of the lithoclastic travertine lithofacies with the massive crystalline and wavy laminated travertine lithofacies is abrupt.

A brownish *banded calcite vein* with a thickness of a few centimeter (ca. 3 cm) (Fig. 5I, J) was observed on the surface of a layer of the massive crystalline travertine. On this surface, the observed vein is broken up and exists as angular, poorly sorted cm–sized pieces. The dipping attitude of this calcite vein is parallel to the one of the massive travertine lithofacies (70° to SW; Fig. 5I–J).

4.2. RMT and ERT measurements

Based on the RMT measurements, resistivity maps (ρ_z; z: elevation above sea level) were compiled, indicating the resistivity distribution at a given horizontal plane. They facilitate the identification of the thickness of the confining layer and the travertine body. This provides the opportunity to evaluate the possible travertine linkage between the quarries. Three electrostratigraphic units (EsU) were distinguished based on the relative frequency of the resistivity values (Fig. 6). The lowest resistivity values (<100 Ωm; EsU I) were detected along the small ridge situated in the northeastern part of the study area and in deeper regions (under 245 m a.s.l.), while the greatest resistivities (>400 Ωm; EsU III) were recorded in the Gazda and Cukor quarries. Transitional resistivity values (100–400 Ωm; EsU II) were detected in the area between the quarries (Fig. 6). In the measured geoelectric profile (ERT) resistivity values range from 50 up to 1000 Ωm. The aforementioned three electrostratigraphic units could also be distinguished within the resistivity profile (Fig. 7). EsU I (<100 Ωm) is the most dominant lateral unit ranging from 80 m till the end of the profile. EsU III (>400 Ωm) forms a triangle–shaped unit in the southwestern edge of the profile wedging out to the northeast. The EsU II, representing a transition zone in–between EsU I and III, forms a narrow, ca. 15 m wide zone around EsU III.

4.3. Micropetrographic characteristics

The Cukor travertine is microscopically characterized by sparitic calcite, showing different crystal sizes, that either forms the matrix or occurs as pore–filling phases. Within the lithofacies, calcite crystals appear in the following shapes and forms (Fig. 8):

(1) *Micritic calcite* develops sporadically in all lithofacies of the Cukor travertine. The small (1–4 μm in size) calcite crystals occur along

Fig. 5. Overview of the most characteristic macroscopic features of the observed lithofacies. (A) Massive crystalline travertine lithofacies interbedded with thin–bedded/laminated crystalline travertine. (B) Coated bubbles within massive crystalline travertine lithofacies indicated by yellow arrows. (C) Dense network of straw–like pores in phytohermal crystalline travertine. (D) Thin–bedded/laminated crystalline travertine lithofacies with characteristic layer parallel pore network. (E) Layers of micro terraces represented by porous horizons on freshly cut surface. (F) Plan view of the porous horizon along which micro-terraces can be observed. (G) Lithoclastic travertine lithofacies consisting of angular clasts of travertine embedded in orange colored weakly cemented carbonate mud. (H) Manganese oxy/hydroxide layer covering calcite encrustation around the clasts in lithoclastic travertine lithofacies. (I) Steeply dipping layers (indicated by the black line) of the massive crystalline travertine towards SW. (J) Thin calcite veneer on the surface of the massive crystalline travertine (location of the calcite veneer indicated by black rectangle in Panel I).

the edges of phyto–mold showing gradual transition into larger crystal forms (Fig. 8A). In some cases, micrite crystals form small (10–30 μm, respectively) isolated clumps and islands embedded in micro– and sparitic calcite crystals (Fig. 8D). In the lithoclastic (breccia) travertine lithofacies, micrite occurs as dense few millimeter sized irregular micritic islands that are surrounded by sparitic calcite (Fig. 8B).

(2) *Calcite micro–spar* ranges between 5 and 20 μm forming a transition between spar and micrite crystals.

(3) *Calcite spar* is represented by equant blocky crystals ranging from 20 up to 150 μm (Fig. 8D–F). This group of calcite crystals is characteristic for the main lithofacies of the Cukor travertine. Two kinds of calcite spar can be distinguished based on micro–features. A group of calcite spars consists of crystals with straight and well-defined boundaries and absence of solid–inclusions, forming the largest volume of the lithofacies in which it both occurs as primary fabrics and as pore–filling cement (Fig. 8B, D, E, F). The other group of calcite spars is defined by wavy and blurry crystal edges as well as their richness in solid inclusions (Fig. 8C).

(4) Elongated, *feather–like calcite* is present in the "micro terraces" lithofacies (Fig. 8G). These feather–like calcite structures are made up of radial crystallites with large variations in orientation showing sweeping extinction under crossed polars. The largest plate–like crystals may reach several millimeter in length. The space between the individual "feathers" are filled with micro–

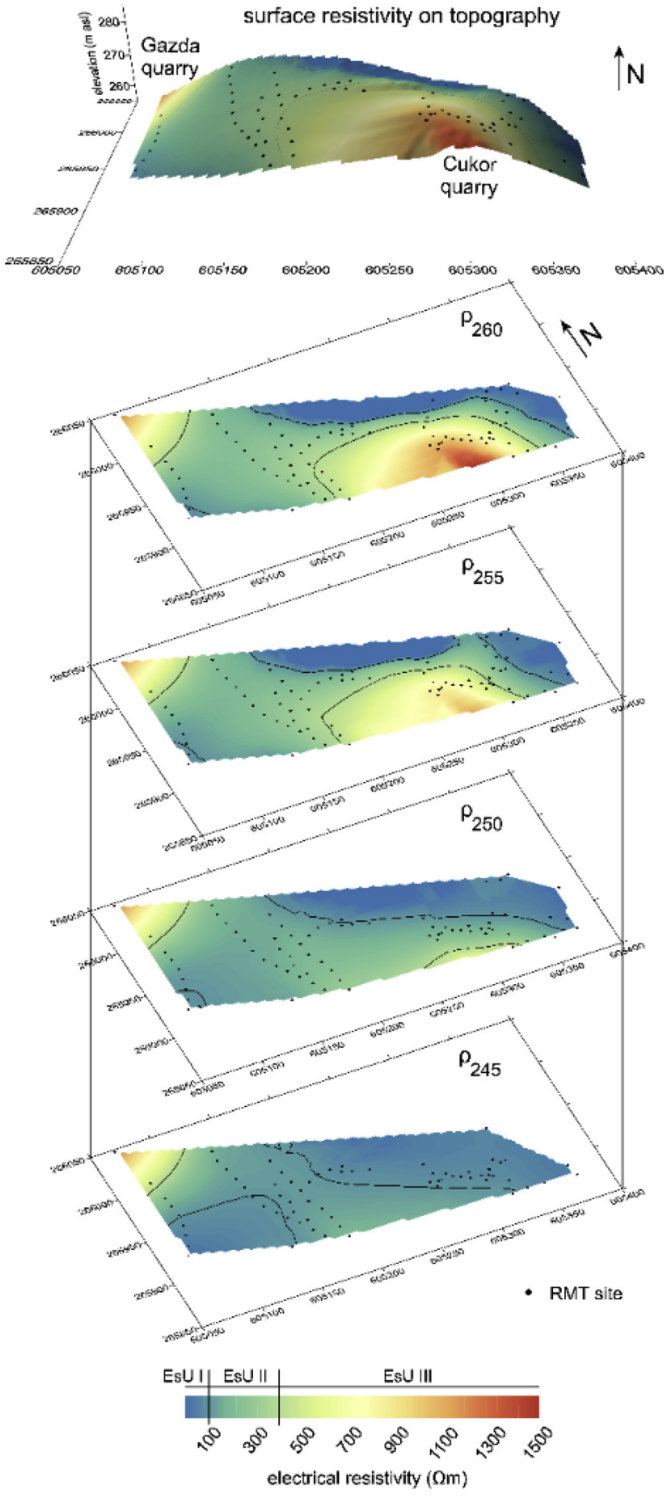

Fig. 6. Resistivity maps at different elevations (ρ, in meter above the sea level) indicating electrostratigraphic units (EsU) based on RMT measurement (EsU I – 0–100 Ωm; EsU II – 100–400 Ωm; EsU III – 400–1000 Ωm).

spar and spar crystals. These structures often show a dense "feather" pattern.

Reworked clasts of the aforementioned calcite fabrics were also observed predominantly within the lithoclastic (breccia) travertine lithofacies (Fig. 5G). Moreover, some extraclasts are present within this lithofacies, such as angular quartz grains and bone-fragments.

Dissolution and decomposition of organic matter are the most significant processes in the formation of porosity and permeability (e.g. Pentecost, 2005) providing space for subsequent fluid circulation inducing calcite precipitation. The most commonly observed pore types are vugs, phytomoldic and interparticle pores, all related to these abovementioned processes (Fig. 8A, B, F). Different kinds of cements can be observed within the pore space. The most characteristic cement types are the equant mosaic cement that partly infills the pore space (Fig. 8A, B). In some cases, bladed calcite cement was also recognized (Fig. 8E). In CL microscope, the primary sparitic calcite crystals are predominantly non–luminescent. However, the inner parts of the crystals is occasionally exhibit dull–luminescent and/or bright–luminescent zones (Fig. 8F). Regular alternation of these zones is rare and mottled luminescence of calcite crystals is sometimes observed (Fig. 8F).

4.4. $\delta^{18}O$, $\delta^{13}C$, Δ_{47} and $^{87}Sr/^{86}Sr$ values

$\delta^{18}O$ and $\delta^{13}C$ values are summarized in Table 1 and Fig. 9 and sample locations are shown in Fig. 3. Full data are provided in supplementary Table S1. Sampling was carried out perpendicular to the bedding as well as along a layer in order to investigate spatial trends in the isotopic composition. The $\delta^{13}C$ data range between −2.6 and 0.3‰ V–PDB, with a mean value of −1.2 ± 1.7‰, whereas $\delta^{18}O$ data range between −13.9 and −11.4‰ with a mean value of −12.9‰ ± 1.0‰ V–PDB.

$\delta^{18}O$ signature of the sparite phase is significantly different (mean value of −13.0‰ ± 0.5), plotting bellow the 75th percentile of the data sets of micro-sparitic phase (Fig. 9B). $\delta^{13}C$ data of the sparite phase show an average of −1.3 ± 0.6‰ (ranging between −2.1 and −0.4‰) having significantly lower carbon isotope signature compared to the values of the micro-sparite phase (Fig. 9C). Contrary to the sparite phase, the micro–sparite phase shows significantly heavier $\delta^{13}C$ signature (−0.4‰ ± 0.4 in V–PDB) whereas $\delta^{18}O$ data represent slightly lighter values (−13.6‰ ± 0.2 in V–PDB) (Fig. 9B, C). Stable isotope data of bulk samples (with a mean value of −1.1‰ ± 0.7 for $\delta^{13}C$ and −12.4‰ ± 0.9 for $\delta^{18}O$ in V–PDB) show overlapping characteristics with the groups of the sparite and micro–sparite phases. There is no significant difference between stable isotope values of the different lithofacies.

Clumped isotope measurements were carried out on one sparitic sample (CU15AT003) from the Cukor quarry in order to determine the temperature of travertine precipitation, and, together with the carbonate $\delta^{18}O$ value, to calculate the $\delta^{18}O$ value of the precipitating fluid. Results of the clumped isotope measurements are summarized in supplementary Table S2, and full data are provided in supplementary Table S2. The determined average Δ_{47} value is 0.618 ± 0.005‰. The corresponding temperature was calculated using the equation of Kelson et al. (2017) resulting in 22 °C (±0.005). The sample used for clumped isotope measurement has a $\delta^{13}C$ value that agrees with the average carbon isotopic value for the Cukor travertine samples in Table 1, but possesses a slightly lower average oxygen isotopic signature. The $\delta^{18}O$ of water calculated from the clumped isotope temperature of 22 °C and $\delta^{18}O$ of carbonate value for sample CU03 is −11.0 ± 0.009‰ (V-PDB). The $\delta^{18}O$ of the water was calculated using the average $\delta^{18}O$ of the sparite-, micro-sparite and bulk phases of the Cukor with application of the equations of Kim and O'Neil (1997), Coplen (2007) and Kele et al. (2015).

The $^{87}Sr/^{86}Sr$ of the Süttő travertine area does not vary significantly between the outcrops (Fig. 10A). Strontium values vary between 0.70835 and 0.70860 with an average value of 0.70848. The samples of the Cukor travertine display an average value of 0.70852, representing a strontium ratio typical for the Süttő travertine area (see Fig. 10A).

4.5. U–Th dating

U-Th sample locations are indicated on Fig. 4A, and the results of the analysis are presented in Table 2. The $^{230}Th/^{232}Th$ ratios suggest that

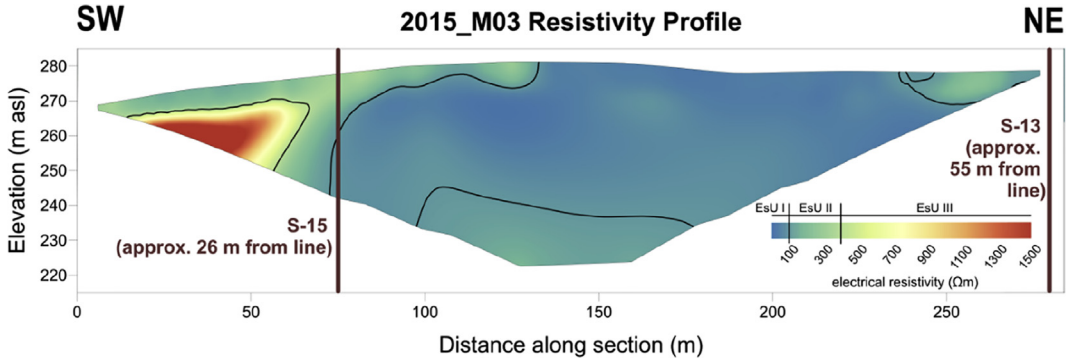

Fig. 7. Geoelectric profile inbetween Gazda and Cukor quarries (see Fig. 2) indicating electrostratigraphic units (EsU) (EsU I – 0–100 Ωm; EsU II – 100–400 Ωm; EsU III – 400–1000 Ωm).

with one exception, the analyzed samples of the Cukor quarry are low in detrital thorium ($^{230}Th/^{232}Th$ <100), therefore detrital correction of these samples was not necessary. However, the sample from the lithoclastic (breccia) lithofacies shows considerable contamination by detrital thorium, therefore age correction was applied. The resulted ages range from 318 ± 18 to 554 ± 60 ka BP (Table 2). The vein sample shows the highest $^{230}Th/^{232}Th$ ratios, i.e. a complete absence of detrital thorium.

5. Data integration and discussion

5.1. Interpretation of travertine lithofacies and fabrics

The observed inclined phytohermal crystalline- and the thin-bedded crystalline facies are indicative of a slope depositional system. The latter is quite similar to the one described from the neighboring Gazda quarry (Török et al., 2017), and to other slope depositional systems documented from many localities around the world (Alçiçek et al., 2017). Depending on the temperature and the saturation of the travertine precipitating fluid(s), plants could have colonized the surface of the prograding travertine slopes, encrusting the stems of the plants thus forming the phytohermal crystalline facies. When precipitation rate increased, plants could not keep up with the fast carbonate precipitation and became buried by layers of thin laminated crystalline crust. The latter precipitated from a carbonate saturated water film flowing along the steep slope. This process and variations in precipitation rate likely caused the observed alternating layers of the phytohermal and the thin laminated facies (see Fig. 4A). Some parts of the slope had suitable conditions for the formation of micro–terraces recognized as redeposited blocks within the lithoclastic travertine facies (Fig. 5E, F). Micro–terraces are common around springs (Geurts et al., 1992; Pentecost, 2005). Depending on the distance between dams, the

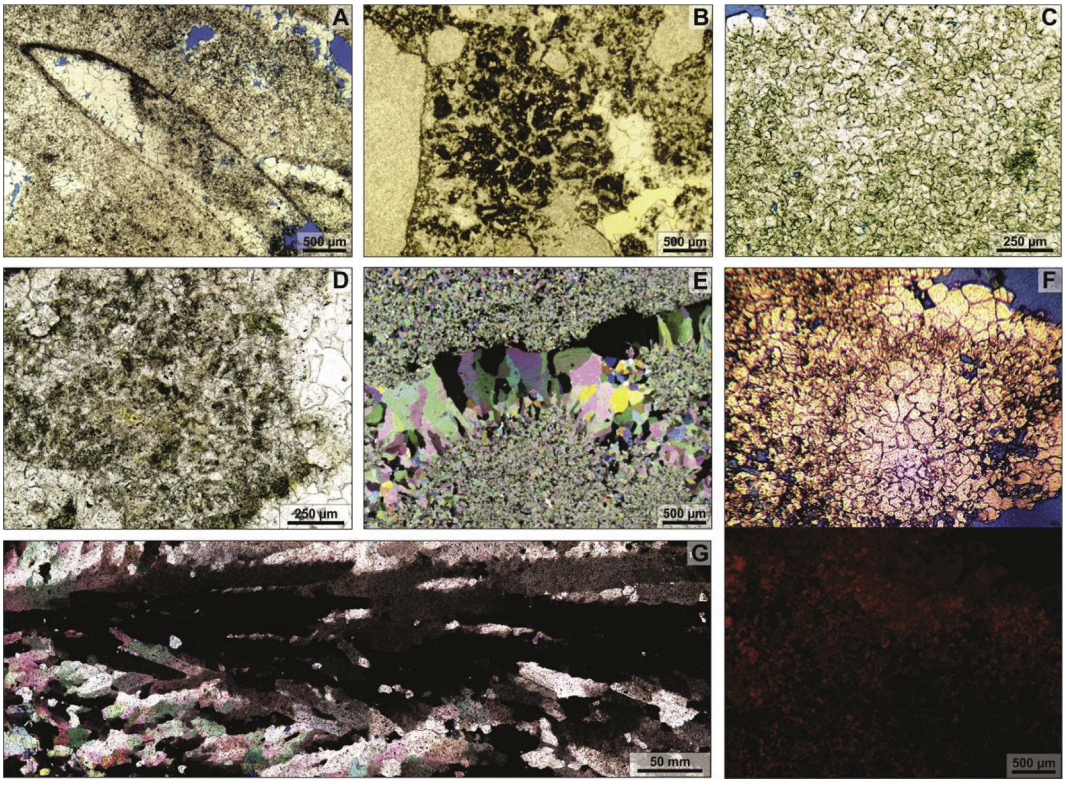

Fig. 8. Micro–features of the identified lithofacies of Cukor quarry. (A) Phytomold filled with blocky calcite cement. Along the edge of the pore, a few micrometers thick micrite coating can be observed (PL photo). (B) Angular clasts of massive crystalline travertine enveloped by thin layer of micrite. Between the angular clasts, islands of dense micrite and calcite cement occur (PL photo). (C) Solid–inclusion rich calcite spar (PL photo). (D) Clotted micrite embedded in sparitic calcite (PL photo). (E) Vuggy pore in massive crystalline crust almost entirely filled with bladed calcite cement (PPL photo). (F) Equant mosaic cement and solid–inclusion rich sparitic calcite showing dull mottled orange luminescence (upper: PL photo; lower: CL photo). (G) Elongated, feathery calcite crystal embedded in sparitic calcite (PPL photo). (PL – polarized light, PPL – cross–polarized light).

Table 1
Summary of $\delta^{13}C$ and $\delta^{18}O$ values of Cukor quarry travertine, from which sparite and micro–sparite phases were separately sampled. Bulk samples represent a mixture of these two phases.

	Number of samples	$\delta^{13}C$ (‰, V–PDB)			$\delta^{18}O$ (‰, V–PDB)		
		Minimum	Maximum	Average	Minimum	Maximum	Average
Sparite phase	11	−2.1	−0.4	−1.3 ± 0.6	−13.5	−12.2	−13.0 ± 0.5
Micro–sparite phase	14	−1.1	0.3	−0.4 ± 0.4	−1,313,134.0	−13.2	−13.6 ± 0.2
Bulk	6	−2.6	−0.6	−1.1 ± 0.7	−13.4	−11.4	−12.4 ± 0.9

steepness of the slope can be identified (Pentecost, 2005). In case of the Cukor quarry, the distance between each dam is about 2 cm suggesting a slope of about 40°.

Carbonate precipitation close to the spring orifice is controlled by fast degassing, resulting in micro–textures with sparite crystals. Since both the primary and secondary carbonate precipitates are characterized by sparite crystals, separation of different calcite generations is difficult, however, some micro–features of the crystals can help in making the distinction. The observed calcite spars represent two groups of different origin. The group with solid inclusion poor sparite crystals which display clear, well–defined crystal edges represent pore–filling cement generations (Fig. 8). These crystals are predominantly non-luminescent reflecting precipitation under oxidizing conditions. The other group of solid inclusion rich calcite spars with wavy and blurred crystal edges represents carbonate precipitates that, later on, were affected by neomorphism, i.e. sparitization. Similar evolution was also observed as recrystallization stages of shrubs by Guo and Riding (1994) and Claes et al. (2017). The solid inclusions could be the remnants of non–carbonate phases (Török et al., 2017). The latter sparite crystals occasionally show mottled luminesce providing additional evidence for recrystallization (Fig. 8F).

The micro–terraces are made of elongated, feathery crystals (Fig. 8G) characteristic of thermogene travertine with high precipitation rates (Guo and Riding, 1992; Pentecost, 2005). Chafetz and Folk (1984) described similar crystals from the Central Italian travertine outcrops as "ray crystals". Based on the texture of the feathery crystals, they can be related to a dominance of physico-chemical precipitation, i.e. fast degassing of highly calcite oversaturated fluids.

In conclusion, micro–terraces and coated bubbles, in particular, are diagnostic fabrics of spring related travertine deposits (Gandin and Capezzuoli, 2014). Additionally, the massive white macro–appearance of the crystalline fabrics, and the micro-scale feathery calcite are typical for fissure ridge travertine deposits (Guo and Riding, 1998). Although some crystalline fabrics can be partly related to recrystallization, careful petrographic observations indicate the existence of primary crystalline fabrics, too. Evidence for the primary origin of the calcite crystals are presented by straight crystal boundaries and transparent – inclusion-free – crystals possessing predominantly non–luminescent characteristics. These suggest fast carbonate precipitation, often in a spring-proximal position, along a self–created slope depositional environment. The observed crystalline textural characteristics of the Cukor travertine body are in contrast with the micrite dominated lithofacies reported

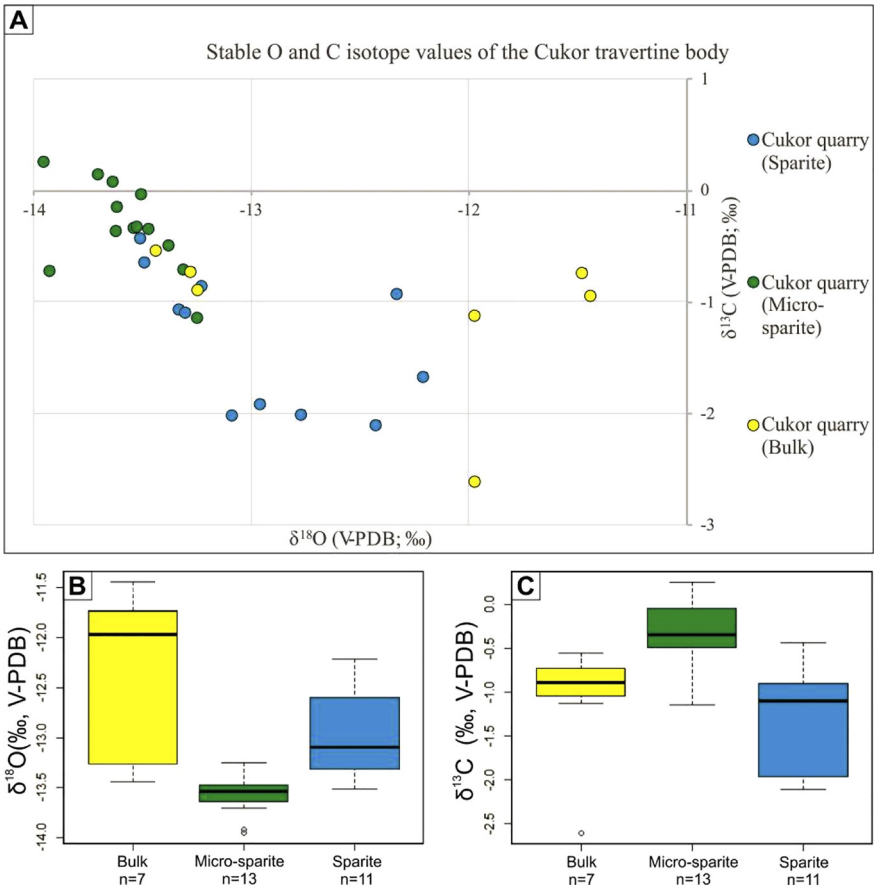

Fig. 9. (A) Cross–plot of $\delta^{13}C$ – $\delta^{18}O$ values of Cukor quarry. (B) Boxplots of the $\delta^{18}O$ values of the bulk, micro-sparite and sparite phases. (C) Boxplots of the $\delta^{13}C$ values of the bulk, micro-sparite and sparite phases. Stable isotope compositions of the micro-sparite and sparite phases are significantly different. Data are displayed as individual points when values are outside the range defined by [Q1 − 1.5*IQR, Q3 + 1.5*IQR].

A

Location	Sample Nr.	$^{87}Sr/^{86}Sr$
Cukor quarry	CU02	0.70847
	CU14	0.70856
Diósvölgy quarry	DV09	0.70850
	DV21	0.70851
Hegyhát quarry	HE01	0.70843
	HE02	0.70845
Óharaszt quarry	OH03	0.70838
	OH04	0.70838
Gazda quarry	GA_Vein	0.70860
	SU_GA14	0.70847
	SU_GA25	0.70847
Újharaszt quarry	UH123	0.70848
Bego quarry	BE02	0.70850
	BE30	0.70849

B

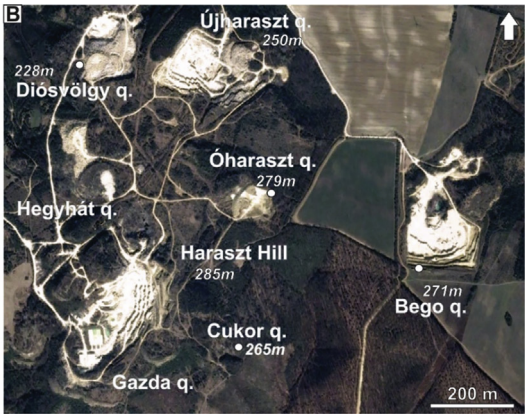

Fig. 10. (A) Strontium isotope values of the Süttő travertine area. $\delta^{87}Sr$ values are uniform. (B) Satellite image of the quarries of the Süttő travertine area with indication of elevation above the sea level.
(Modified after Google Maps.)

from the neighboring outcrops (Sierralta et al., 2010; Török et al., 2017) suggesting that the Cukor travertine body is a unique depositional environment, where one of the ancient springs of the Süttő travertine might have been located.

5.2. Geophysical methods as powerful tools for mapping morphotectonic features in travertine depositional systems

On the basis of the lithological succession exposed in the quarries and boreholes at Süttő, it is obvious that the beds overlying and underlying the travertine body have significantly lower resistivity values than those characterizing the travertine itself (Loke et al., 2013). This allows a relatively straightforward mapping of the intact travertine body by electric and electromagnetic methods, in this case RMT and ERT. In fact, after correlation of the resistivity values with the available borehole information (Véghné et al., 1971), field observations (Fig. 3) and literature analogues (e.g. Palacky, 1988), EsU III corresponds unequivocally to travertine. Likewise, EsU I represents fine-grained siliciclastic sediments such as loess and sand. EsU II (with transitional resistivity values) could be interpreted as coarser-grained sediments of travertine and/or loess and sand. The data set provided by RMT measurements allows preparation of resistivity maps of the near subsurface region (0–50 m). Based on these maps the highest elevation of the Cukor quarry is around 275–280 m (a.s.l.). The resistivity map of the level at 245 m (a.s.l.) (ρ_{245} map; Fig. 6) shows absence of travertine, suggesting that the maximum vertical extent of travertine here ranges between 30 and 35 m. Additionally, all ρ_z maps indicate two separated travertine bodies, present in the left upper and right lower corners on the map. It indicates that the travertines exposed by the Gazda and Cukor quarries are disconnected. Furthermore, the antecedent topography of the travertine body, displaying the pre-travertine relief can also be identified (Fig. 11A). It can be concluded that the antecedent topography was already developed at the time of the Cukor travertine formation i.e. the topographic height of the Haraszt Hill was already present when travertine deposition began. On its southern slope a local depression was present providing accumulation space for the formation of the Cukor travertine. Additionally, on the western slope of the edge of Haraszt Hill another depression can be seen, suggesting the formation of the Gazda travertine body also having taken place in a depression.

The geoelectric profile across the Haraszt Hill (Figs. 3, 7 and 11B) shows a triangle–shaped travertine body in the south-western edge of the profile, wedging out to the northeast. The surrounding boreholes (S–13 and S–15, in Figs. 2B and 3) did not intersect travertine, indicating that the Cukor travertine wedges out towards the NE. The abrupt boundary between the travertine and non–travertine lithologies suggests a tectonic contact.

In conclusion, ERT and RMT measurements, in combination with borehole data, facilitated the identification and 3D mapping of travertine and tectonic structures in the subsurface. The travertine consists of an isolated domal geobody in continuation with the surface outcrops with a maximum thickness of 35 m. It developed along the south–eastern slope of the Haraszt Hill in a depressional paleo–topographical setting.

5.3. Depositional temperature and origin of the parent fluid(s)

$\delta^{18}O$ and $\delta^{13}C$ values of the travertine body cluster around −13.1‰ and −0.9‰, respectively (Table 3). These signatures are diagnostic for thermogene (Pentecost, 2005) or hypogean (Teboul et al., 2016) travertine deposits, precipitated from dominantly “endogene” (i.e. deep ground) waters (Crossey et al., 2006). The $\delta^{13}C$ values of the travertine reflect the $\delta^{13}C$ value of the fluid source as well as the carbon signature of the porous rock through which the fluid was flowing. Possible CO_2 sources are summarized in Fig. 12. Using the empirical equation of Panichi and Tongiorgi (1976), the $\delta^{13}C_{CO2}$ of the precipitating waters can be calculated. In the case of the Cukor travertine this value plots around -12 ± 2‰ suggesting that, beside the main carbon source (i.e. dissolution of Triassic and Jurassic carbonate successions forming the dominant part of the Gerecse Hill, e.g. Haas, 2001), some CO_2 contribution originated from the atmosphere, from soil and from deeply circulating fluids (Fig. 12). This observation is in full accordance with previous studies carried out in the area (Sierralta et al., 2010; Török et al., 2017).

While the $\delta^{13}C$ value is comparable to the results acquired from the rest of the Süttő travertine area (Török et al., 2017), the $\delta^{18}O$ of the Cukor travertine is generally lower (Fig. 13). The lower $\delta^{18}O_{trav}$ can be explained by either a source of lower $\delta^{18}O_{water}$ and/or a higher precipitation temperature. Although the U-Th data indicate a different fluid episode in comparison to the rest of the Süttő travertine area, based on the stable carbon isotope signature, the main fluid reservoir seems not to have changed between the two episodes.

Estimation of the precipitation temperature is challenging due to the processes of carbonate formation where kinetic fractionation frequently occurs. Vent and pool depositional environments are the ‘closest-to-equilibrium’ places where temperature calculation can be done with the least error (Yan et al., 2012; Kele et al., 2008, 2011, 2015).

For paleo-temperature calculation, equations of Kim and O'Neil (1997), Coplen (2007) and Kele et al. (2015) were used (Table 3). $\delta^{18}O$ of the travertine precipitating fluid was calculated using the temperature derived from the measured Δ_{47} value and the above equations, which are based on the temperature dependence of calcite-water oxygen isotope fractionation (Table 3). Based on the $\delta^{18}O$ of the travertine precipitating fluid, precipitation temperature of the different calcite phases (i.e. sparite and micro-sparite phases) can be calculated. The

Table 2
U-series results of the Cukor quarry. The error is 2σ.

Sample number	^{238}U		^{232}Th		$^{230}Th/^{232}Th$		$^{230}Th/^{232}Th$		$\delta^{234}U$[a]		$^{234}U/^{238}U$		$^{230}Th/^{238}U$		$^{230}Th/^{238}U$		Age (yr ago)		$\delta^{234}U_{initial}$[b]	
	(ng/g)		(pg/g)		(atomic × 10^{-6})		(activity)		(measured)		(activity)		(activity)		(activity)		(uncorrected)		(corrected)	
CU15AT001	4,6	±0,01	11,5	±7,7	12,366	±8296	**±2308,3**		673	±12	1,7	1,01	1,9	±0,02	±97,0	±0,9	450	±48,719	**450**	**±48,715**	2396	±405
CU15AT004	8,4	±0,02	9157	±35	21,60	±0,61	±4,0		352,9	±7,4	1,4	1,01	1,4	±0,04	±72,8	±2,1	369	±73,201	**354**	**±64,063**	957	±237
CU15AT014	7,4	±0,02	9,9	±7,4	15,311	±11,449	**±2858,1**		236,5	±7,6	1,2	1,01	1,2	±0,01	±63,4	±0,5	318	±17,676	**318**	**±17,674**	580	±36
Cukor Vein	686,1	±1,1	147,0	±8,0	77,202	±4216	**±14,411,0**		6,8	±1,7	1,1	1,00	1,0	±0,00	±51,2	±0,1	554	±60,140	**554**	**±60,137**	32	±11

[a] $\delta^{234}U = (^{234}U/^{238}U_{activity} - 1) \times 1000$.
[b] $\delta^{234}U_{initial}$ was calculated based on ^{230}Th age (T), i.e., $\delta^{234}U_{initial} = \delta^{234}U_{measured} \times e^{\lambda 234 \times T}$.

resulting $\delta^{18}O_{water}$ values were then compared to the $\delta^{18}O_{water}$ values provided by Babidorics et al. (1998) in order to select the most plausible $\delta^{18}O_{water}$ values for the Pleistocene waters. According to Babidorics et al. (1998) the ground waters infiltrated in Pleistocene times in the thermal karst system of the Buda Mountains (Hungary) are characterized by a $\delta^{18}O$ range of −14‰ to −11‰, whereas the thermal waters have $\delta^{18}O$ values between −12.7‰ and −9.4‰ (V-SMOW). Our U-Th dating reveals that the Süttő travertine area was active during Pleistocene, in agreement with Kele (2009) and Sierralta et al. (2010). Consequently, the travertine precipitating fluids could have been characterized by a similar $\delta^{18}O$ range as the waters in the Buda Mountains represented by an oxygen isotopic range from −14‰ to −9.4‰ (V-SMOW), supposing a combination of karstic and thermal water origins. Our calculations, using the equation of Kim and O'Neil (1997), resulted in a $\delta^{18}O_{water}$ value of −9.3‰ (V-SMOW), which is out of the above range. The equation of Kele et al. (2015) suggests karstic water origin with calculated value of −12.3‰ (V-SMOW) whereas equation of Coplen (2007) resulted $\delta^{18}O_{water}$ signature of −10.9‰ (V-SMOW) with dominance of thermal water contribution. In all cases, equilibrium is assumed.

Using the calculated $\delta^{18}O_{water}$ signatures (indicated in the second column of Table 3) and considering the $\delta^{18}O_{water}$ ranges provided by Babidorics et al. (1998) (indicated in the last column of Table 3), the temperatures of all Cukor travertine samples could be calculated (Table 3). Depending on the applied $\delta^{18}O_{water}$ value, the micro-sparitic calcite phase is characterized by the highest calculated precipitation temperature ranging between 34 and 36 °C, while the sparite phase could have precipitated from slightly colder fluids (31–32 °C). Our calculations demonstrate that the derived temperatures only slightly depend on the equation used in the calculations. Comparing the results of this study with the one published on the neighboring Gazda quarry (Török et al., 2017) (Fig. 13 and Table 3), it can be stated that the temperature of the precipitation fluid must have been at least 7 °C higher in case of both sparite and micro-sparite phases of the Cukor travertine than in the case of the Gazda travertine body.

On the basis of the $^{87}Sr/^{86}Sr$ ratios there is no significant difference between the values of the Cukor travertine and the neighboring travertine body exposed in the Gazda quarry (Fig. 10). This suggests that even though these travertine bodies show petrographic differences and were formed in isolated depositional environments, the travertine precipitating fluids originated from the same reservoir. The Sr signatures of the travertine deposits of the Süttő area, however, are significantly higher than those of either the Upper Triassic (0.7076–0.7080) or the Eocene (0.7077–0.7078) marine carbonates forming the dominant part of the reservoirs in the Transdanubian Range (e.g. Brass, 1976). This indicates that the travertine precipitating fluid(s) also could have interacted with other rock sequences with higher $^{87}Sr/^{86}Sr$-ratios (e.g. McArthur et al., 2001). Based on the local geology, Paleogene (i.e. Oligocene) siliciclastic rocks, characterized by higher $^{87}Sr/^{86}Sr$-ratios are likely candidates, because they occur in the Süttő area directly underneath the travertine and on top of the Mesozoic and Paleogene successions. Given the uniform signature, leaching of Sr with high $^{87}Sr/^{86}Sr$-ratios from these Oligocene lithologies might have happened during (downward) percolation of the fluids.

In conclusion, stable and clumped isotope data suggest that the Cukor travertine precipitated from waters coming from the same main reservoir, although precipitation temperature was most likely higher than the one inferred for the other nearby travertine deposits (Fig. 13). This supports the idea that the area of the Cukor quarry was a discharge center of the travertine depositing springs. Additionally, the travertine precipitating fluids interacted not only with Upper Triassic and Eocene marine carbonate successions but also with Oligocene siliciclastic rocks, resulting in a mixed $^{87}Sr/^{86}Sr$ signature.

5.4. The age of the travertine body

The age of the Süttő travertine complex has been estimated by several methods resulting in several independent age ranges (Ruszkiczay-Rüdiger

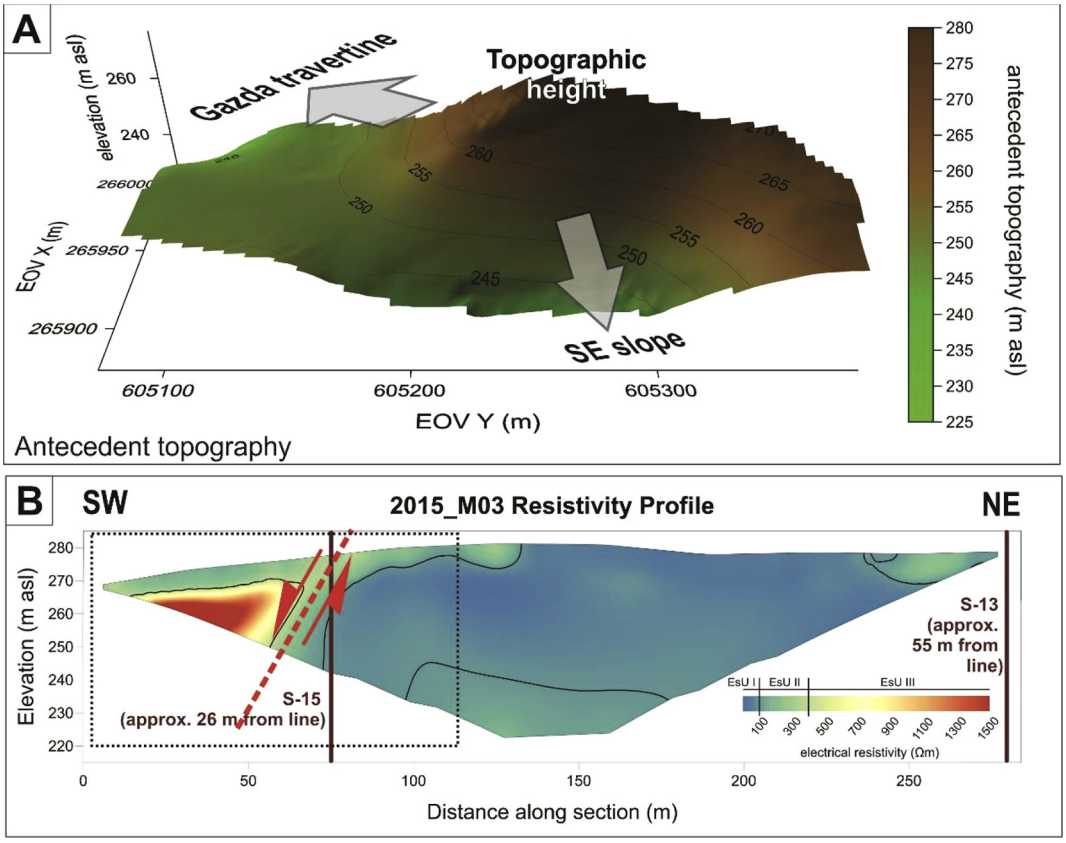

Fig. 11. Results of the geophysical measurements in the Cukor quarry and its surroundings. (A) Antecedent topography map of the Cukor travertine and its surroundings indicating that by the time of the Cukor travertine formation there existed already a slope towards the valley of the Gazda travertine and another one towards SE, to the valley of Bikol creek. The travertine formation could have taken place along the latter. (B) Resistivity profile confirming the presence of a NW–SE normal fault which may have acted as a fluid path for carbonate saturated waters inducing travertine formation.

et al., 2005). The new results have been compared with the previous dating results (Fig. 14) in order to verify the simultaneous deposition of the Cukor travertine body and the other neighboring travertine deposits in the area.

Micro–petrographic analyses revealed that the samples selected for U-series dating were crystalline with a dominance of calcite (>99%). The $^{230}Th/^{232}Th$ atomic ratios confirm the purity of the samples with low contamination as inferred from thorium concentrations that normally are detrital in origin ($^{230}Th/^{232}Th$ <100, Richards and Dorale, 2003; Woodhead et al., 2006). Diagenetic overprint of the primary sparitic calcite generation, as well as the cementation, has been observed to affect the initial uranium and thorium content of travertine (Livnat and Kronfeld, 1985). Due to this, samples with clear indication of recrystallization were avoided as far as possible. To test the level of thorium contamination a sample was taken from the lithoclastic (breccia) travertine facies that apparently formed via the reactivation of the NW–SE directed normal fault after travertine formation (Fig. 6). Since its micro–petrographic characteristics suggest weathering and micritization, leaching of uranium is likely to result in an older age in such a sample (Clark et al., 1991). The older age of the lithoclastic (breccia) travertine facies can indeed be interpreted as a result of uranium leaching due to subaerial exposure and can be considered as an outlier. Based on the remaining data, the formation of Cukor travertine started about 553 ± 60 ka and continued until about 318 ± 18 ka. The U-Th age data provided by Kele (2009) and Sierralta et al. (2010) represent

Table 3
Calculation of the oxygen isotope compositions and temperatures of the travertine precipitating fluid(s) based on clumped isotope measurement. The blue bar on the right indicates the $\delta^{18}O$ range of the karstic waters, whereas the pink bar shows signal of the thermal waters in the Pleistocene times (based on Babidorics et al., 1998). Temperatures as well as $\delta^{18}O_{water}$ signatures within these ranges are accepted as potential values of the travertine precipitating fluid(s).

	Calculated $^{18}O_{water}$ (V-SMOW)	Cukor quarry			Gazda quarry *(Török et al., 2017)*	Range of:	
		Sparite phase	Micro-sparite phase	Bulk	Average	Karstic waters	Thermal waters
Measured $^{18}O_{calcite}$ (V-PDB)		−13.0	−13.6	−12.4	−10.8	*(Babidorics et al., 1998)*	
T°C *(Kim and O'Neil, 1997)*	−9.3	32	35	29	22		
T°C *(Coplen, 2007)*	−10.9	32	36	29	22		
T°C *(Kele et al., 2015)*	−12.3	31	34	28	22		
T°C (47)	22						

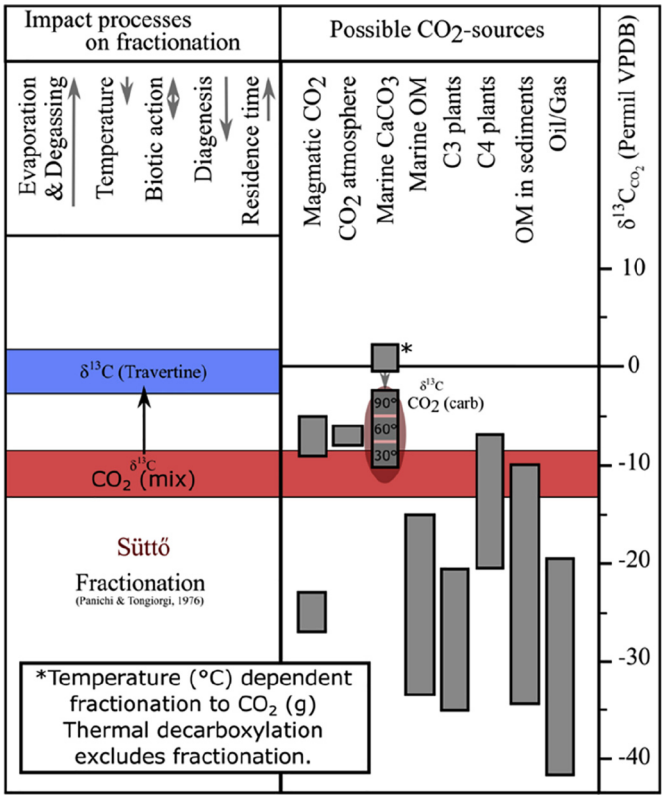

Fig. 12. Possible carbon dioxide sources and related processes related to the $\delta^{13}C$ signatures of travertines (adapted based on Claes et al., 2015; data from Deines et al., 1974; Inoue and Sugimura, 1985; Andrews et al., 1993, 1997; Rollinson, 1993; Sano and Marty, 1995; Rose and Davisson, 1996; Minissale et al., 2002; Minissale, 2004; Sharp et al., 2003; Leng and Marshall, 2004; Attanasio et al., 2006; Uysal et al., 2007; Hoefs, 2009; Jeandel et al., 2010). Temperature dependent fractionation of marine carbonates based on Bottinga (1968) and Friedman and O'Neil (1977). Empirical fractionation from $\delta^{13}C(CO_2mix)$ to $\delta^{13}C$(travertine) based on Panichi and Tongiorgi (1976). Arrows of impact processes are not to scale. Blue bar indicates the carbon isotopic composition of the Süttő travertine complex whereas the red bar shows the range of the calculated carbon isotope values of the CO_2 based on the method of Panichi and Tongiorgi (1976).

younger ages for the travertine formation in the area with a maximum interval of 444–144 ka (including errors) based on samples from the Diósvölgy, Hegyhát and Újharaszt quarries (Fig. 10B).

The age of the travertine body was also estimated based on the fossil content of the Cukor quarry (Pazonyi et al., 2014), which suggests that its formation started much earlier, during the Pliocene – Early Pleistocene (Fig. 14). However, this apparent discrepancy in age can possibly be interpreted by supposing the re-deposition of older fossils. Taken together, the new and previously published age data of the Süttő travertine area (Lantos, 2004; Kele, 2009; Sierralta et al., 2010; Pazonyi et al., 2014; Ruszkiczay-Rüdiger et al., 2018) indicate that the Cukor travertine body must have formed during an independent precipitation phase and represents the oldest deposit of the Süttő travertine complex (Fig. 14).

5.5. The Cukor deposit as a fissure ridge–type travertine body: integration of the results

The steeply dipping travertine beds exposed in the Cukor quarry, coupled with the opposite dip of the beds on the northern and southern parts of the outcrop (e.g. Fig. 4), strongly suggest deposition from thermal spring(s) aligned along the apical part of a fissure ridge (Fig. 15). The fact that this part is now characterized by lithoclastic (breccia) travertine suggests that the fault zone, along which fluids where channeled, also was active after the formation of the fissure ridge. Travertine lithoclasts are bordered with calcite cements attesting a hydrothermal circulation coeval with deformation of the pre-existing travertine. The elongated shape of the travertine body, the nearly parallel subvertical beds forming the opposing slopes, as well as the occurrence of banded calcite veins following the same trend of the whole body strengthens the hypothesis of a NW–SE oriented fissure ridge, now dismantled. Its occurrence and geomorphology indicate a buried fault zone, which played the role of the feeder conduit for thermal springs (Figs. 4, 5). The micro–terraces and coated bubble facies are diagnostic proximal travertine fabrics (Gandin and Capezzuoli, 2014). In addition, the massive white macro-appearance of the crystalline fabrics and the micro–scale feather-like calcite indicate fast carbonate precipitation, typical for fissure ridge travertine deposits (Guo and Riding, 1998). The isolation of the travertine body is confirmed both in space (surface and subsurface mapping) and time (oldest U-Th age). The stable and clumped isotopes suggest a higher precipitation temperature from the same reservoir for Cukor travertine compared to the rest of the Süttő travertine complex. The central fissure of the ridge was highlighted by geophysical data (Fig. 11B). By these analyses, the northern wall of the ridge is topographically higher and its layers are steeper than those of the southern one (Fig. 4). In addition, the geoelectric profile shows a steep boundary between the travertine body and its substratum (Fig. 11B). These observations attest that the original fissure ridge could have been slightly asymmetric, as documented in other areas where fissure ridges developed along the traces of normal faults (i.e. Terme S. Giovanni, Italy; Denizli area, Turkey; Brogi and Capezzuoli, 2009; Brogi et al., 2014b, 2016b). In this view, the fault along which the Cukor fissure ridge developed was characterized by a dominant normal movement with the northern part of the deposit corresponding to the fault–hanging wall (Figs. 4, 15, 16).

Several observations indicate that the original attitude of the travertine beds was modified due to fault activity after their deposition: a) the micro–terraces that developed in the southern wall of the fissure ridge are tilted (Fig. 5E–F); b) the two sides of the ridge display different dip values (Fig. 4A); and c) lithoclastic (breccia) travertine in the central zone of the quarry, in the apical area, can be the result of a brittle deformation of the travertine deposited over the buried fault (Fig. 4A): in this view the lithoclastic (breccia) travertine is interpreted as the result of fault activity after the travertine formation. Alternatively, such lithofacies might be the result of the collapse of some parts of the fissure in correspondence with the central fissure. A similar complex origin of a travertine breccia was described in case of a Slovakian ridge by Gradziński et al. (2014). Clasts of the lithoclastic lithofacies ranging from 0.5 up to several centimeters are partially cemented and float in a weakly consolidated carbonate mud. The occurrence of loess and/or carbonate rich soil filling the open fractures suggests an episode of subaerial exposure of the whole structure after hydrothermal fluid circulation ceased. In conclusion, the formation of the lithoclastic travertine is polygenetic and was the result of the combination of tectonic and sedimentary processes.

The results of the different methods complement each other, allowing the unequivocal reconstruction of the whole Cukor travertine body, and also its feeding system. The conceptual model displaying its evolution is illustrated in Fig. 16.

5.6. Local geological framework and the Cukor fissure ridge

The Cukor fissure ridge developed along a NW–SE trending normal fault that is interrupted, and locally dissected, by NE–SW trending fractures (Fig. 16). This setting fits into the tectonic evolution of the Transdanubian Range and the Pannonian Basin. According to Wéber and Süle (2014) and Wéber (2016), seismic activity in the central part of the Pannonian Basin is regarded as moderate. Looking at the Gerecse Hills (Fig. 2A), the two main fault systems are: (1) NE–SW trending strike–slips and normal faults, formed in a time interval between late Miocene to Present, and (2) NW–SE trending normal faults, which

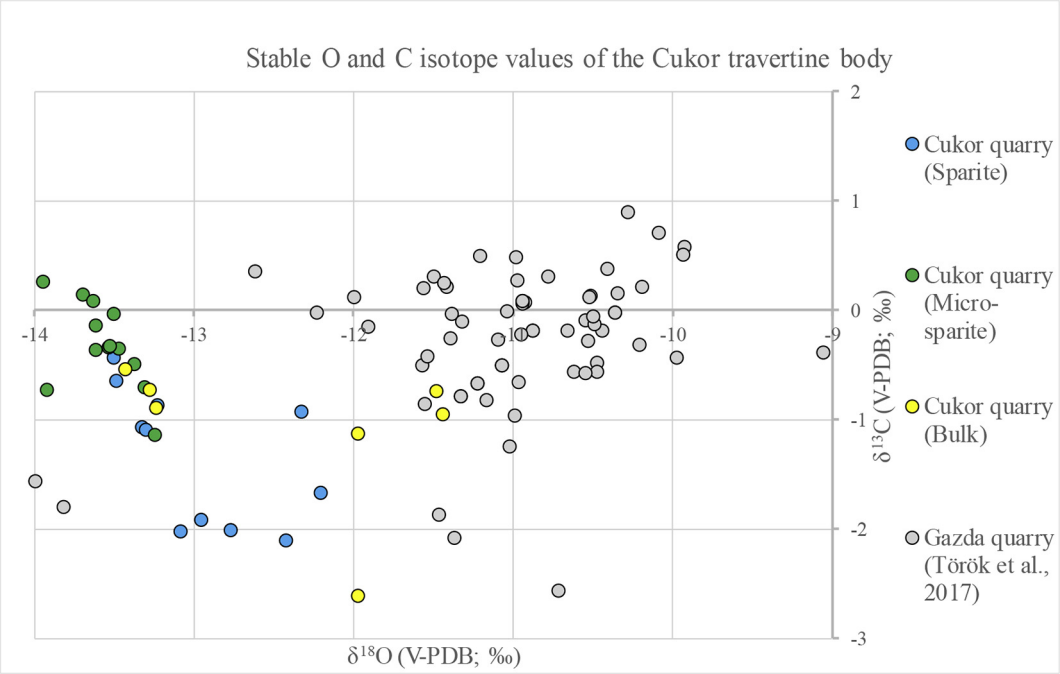

Fig. 13. Cross–plot of $\delta^{13}C$–$\delta^{18}O$ values of the Cukor travertine with indication of the values from the neighboring Gazda quarry (based on Török et al., 2017).

were active during the Cretaceous–Cenozoic time span. Faults of the study area (Figs. 15, 16) show both of these trends as reported in Fig. 2A. However, different ages can be deduced on the basis of this study: as documented by the new U-Th results (Fig. 14, Table 2) deposition of the Cukor fissure ridge can be constrained to a time interval between about 554 ± 60 and 318 ± 18 ka. This constraint implies that the NW–SE trending fault system must have been active, at least in the study area, also during the Middle Pleistocene, right before providing the structural path for the travertine precipitating fluid. Field observations reveal that the NE–SW trending fractures post-date the formation of the Cukor fissure ridge (Fig. 16), suggesting reactivation of this fault population and post-dating the fault system of NW–SE orientation. Travertine precipitation cannot be ascribed to the NE–SW trending fractures in the case of the Cukor fissure ridge. Török et al. (2017) described a NNE–SSW trending fault system from the neighboring Gazda quarry, strictly controlling the travertine deposition. These findings suggest that the regionally observed NE–SW trending fault system was reactivated after the NW–SE trending normal faults, and that these fractures also acted as pathways for travertine precipitating fluid(s) outside of the Cukor fissure ridge.

6. Conclusions

This study presents a multi–methodological approach to reconstruct an eroded, dismantled and buried fissure ridge system and its fault network. Combined stratigraphical and sedimentological

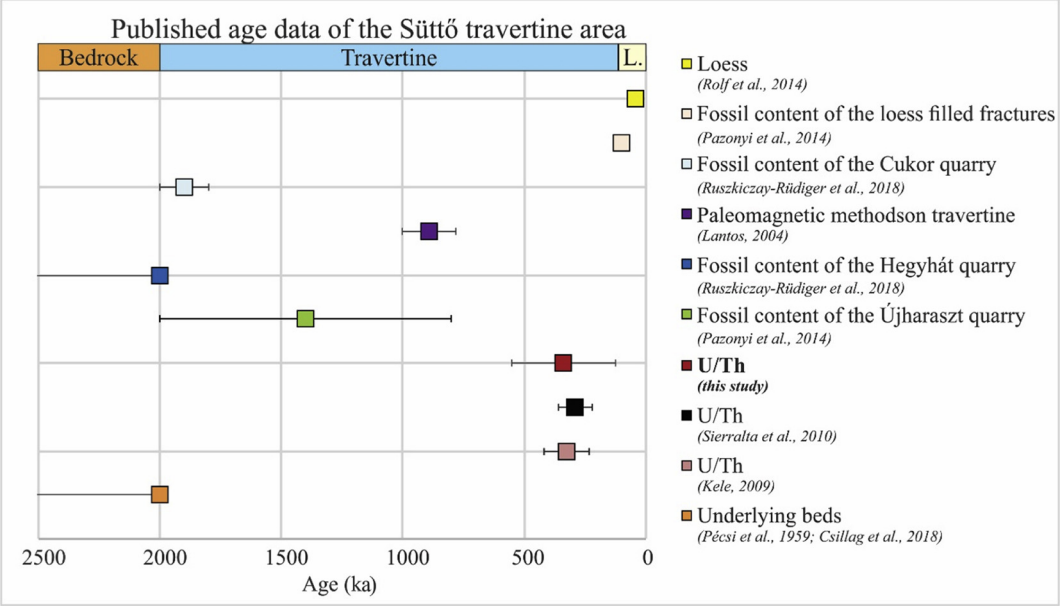

Fig. 14. Age intervals of the bedrock, travertine and the covering loess in the Süttő travertine complex based on published data. Notice that the fossil content of the travertine suggests a longer formation period compared to the U-Th ages.

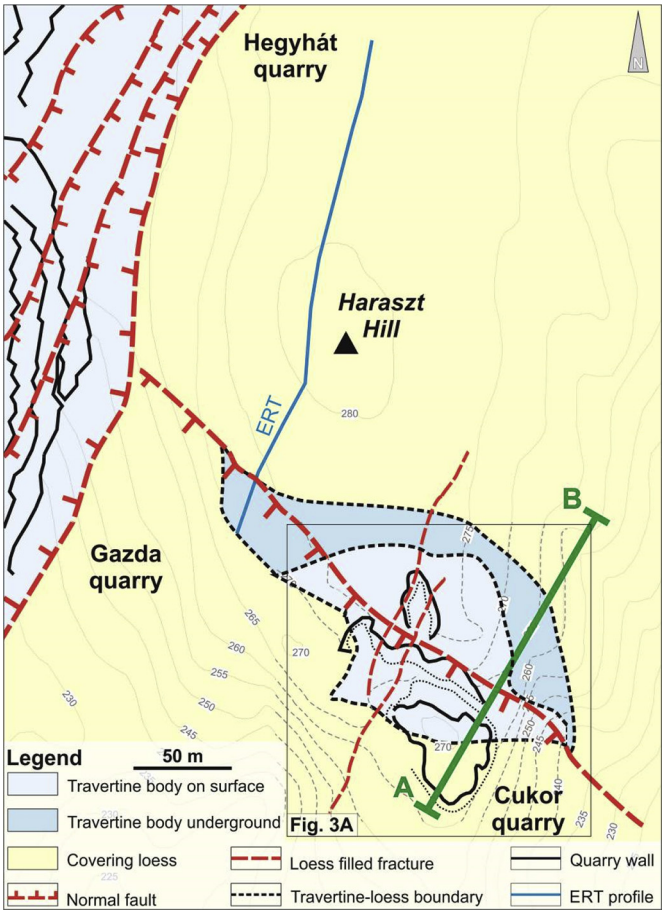

Fig. 15. Map of the Cukor quarry and its surroundings with indication of the observed fractures as well as location of ERT measurement. The green line indicates the location of the cross–section (see in Fig. 11B). The rectangle around the Cukor quarry indicates the location of the sketch map including all field observations (see Fig. 4A).

analyses and mapping of the travertine deposits represent the first step of the approach. Lithofacies distribution and isotope geochemistry helped to reconstruct the paleo-thermal spring location (s) revealing the occurrence of supposed buried faults. Clumped isotope data were used to determine the temperature of deposition and the $\delta^{18}O$ of the paleo-springs. Geophysical data (combination of RMT and ERT) allowed us to delineate the geometry of the non–exposed travertine body and confirmed the existence of the related buried tectonic structures. The methodological approach that was tested here for the Cukor fissure ridge is recommended for use in other areas showing similar exposure conditions, buried faults and related geothermal systems. Reconstruction of buried travertine bodies with this integrated approach can provide insights into older landscapes (maybe even older than Pleistocene) that lack preservation or would no longer be immediately recognized at the surface. The results of this study can be summarized as follows:

- Radiomagnetotellurics (RMT) reveal that the Cukor travertine body was formed in a local depression of the southern slope of Haraszt Hill, and that the maximum thickness of the fissure ridge was 35 m. The Cukor and Gazda travertine bodies are disconnected, suggesting that the Cukor travertine formed in an isolated depositional environment of the Süttő travertine complex. Geoelectric profiles (ERT) confirm the presence of a NW–SE directed normal fault which served as fluid–pathway for the water supply supersaturated with respect to carbonates.
- The Cukor fissure ridge developed along a major NW–SE trending fault, active (at least) during the middle Pleistocene. It could be interpreted as a reactivated fault segment belonging to the Cretaceous–Cenozoic normal fault system in this sector of the Pannonian Basin.
- U-Th dating shows that travertine formation (and the reactivation of the NW–SE directed normal fault) started about 553 ± 60 ka ago and continued until about 318 ± 18 ka ago, suggesting that the Cukor fissure ridge is the oldest member of the Süttő travertine complex.
- Although the Cukor spring, in accordance with the isolated position of the fissure ridge, was not a direct source of the extensive travertine body of Süttő. Stable carbon and strontium isotope measurements reveal that the travertine precipitating fluid of the Cukor travertine had the same origin as those of all the other neighboring travertines in the Süttő travertine area.
- Oxygen isotopic composition of the travertine precipitating fluid was calculated based on clumped isotope temperature values. The calculated precipitation temperatures of the Cukor fissure ridge suggest that the fluid was at least 7 °C higher (between 28 and 36 °C) than that of the neighboring Gazda travertine.

Acknowledgements

The authors are grateful to Tibor Adamcsik (Reneszánsz Ltd.) and his colleagues for their help during fieldwork. Geomega Ltd. (Hungary) is

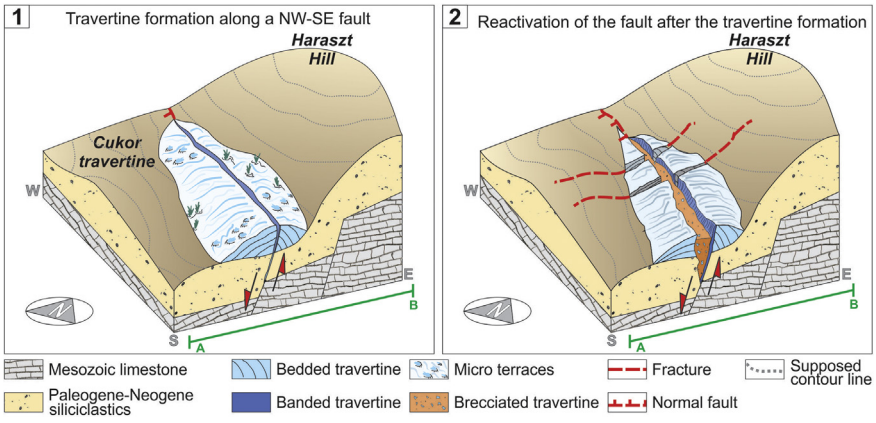

Fig. 16. Evolution model of the Cukor travertine fissure ridge. (1) Travertine formation was taking place along a NW–SE oriented normal fault on the south–eastern slope of the Haraszt Hill. (2) After the formation of the fissure ridge, the normal fault continued its activity producing the displacement of the southern wall of the fissure ridge, as well as the formation of brecciated travertine along the fault zone. NE–SW oriented fractures could have taken place at this time.

thanked for the geoelectric profiling as well as Zs. Zalai, O. Győri, Z. Nagy, T. Müller and M. Temes for their help in the field. László Fodor (MTA–ELTE, Hungary) is also thanked for helpful scientific discussions. Help of A. Schauer and L.K. Burgener (University of Washington Seattle, USA) is appreciated in the course of the clumped isotope measurements and to T. Yu for the U-Th measurements. Enrico Capezzuoli is thanked for the fruitful discussion on the fissure ridge setting. The authors are also grateful to TOTAL, SHELL and PETROBRAS for partial funding of this project. U-Th dating was supported by the Science Vanguard Research Program of the Ministry of Science and Technology (MOST) (106-2628-M-002-013 to C.-C.S.), the National Taiwan University (105R7625 to C.-C.S.), and the Higher Education Sprout Project of the Ministry of Education, Taiwan ROC (107L901001 to C.-C.S.). S. Kele was supported by the National Research, Development and Innovation Office in Hungary (NKFI Alap, KH-125584 project) and by the European Union and the State of Hungary, co-financed by the European Regional Development Fund in the project of GINOP-2.3.2-15-2016-00009 'ICER'.

Appendix A. Supplementary data

Supplementary data to this article can be found online at https://doi.org/10.1016/j.geomorph.2019.106836.

References

Alçiçek, M.C., Alçiçek, H., Altunel, E., Arenas, C., Bons, P., Brogi, A., Capezzuoli, E., de Riese, T., Della Porta, G., Gandin, A., Guo, L., Jones, B., Karabacak, V., Kershaw, S., Liotta, D., Mindszenty, A., Pedley, M., Ronchi, P., Swennen, R., Temiz, U., 2017. Comment on "First records of syn–diagenetic non–tectonic folding in Quaternary thermogene travertines caused by hydrothermal incremental veining" by Billi et al. Tectonophysics 700–701 (2017) 60–79. Tectonophysics 721, 491–500.

Altunel, E., Hancock, P.L., 1993a. Active fissuring and faulting in Quaternary travertines at Pamukkale, western Turkey. Z Geomorph NF 94, 285–302.

Altunel, E., Hancock, P.L., 1993b. Morphology and structural setting of Quaternary travertines at Pamukkale, western Turkey. Geol. J. 28, 335–346.

Altunel, E., Karabacak, V., 2005. Determination of horizontal extension from fissure-ridge travertines: a case study from the Denizli Basin, southwestern Turkey. Geodin. Acta 18, 333–342.

Andrews, J.E., Riding, R., Dennis, P.F., 1993. Stable isotopic compositions of recent freshwater cyanobacterial carbonates from the British Isles: local and regional environmental controls. Sedimentology 40, 303–314.

Andrews, J.E., Riding, R., Dennis, P.F., 1997. The stable isotope record of environmental and climatic signals in modern terrestrial microbial carbonates from Europe. Palaeogeogr. Palaeoclimatol. Palaeoecol. 129, 171–189.

Attanasio, D., Brilli, M., Ogle, N., 2006. The Isotopic Signature of Classical Marble: Rome, Ed. L'Erma di Bretschneider 297 p.

Babidorics, J., Fórizs, I., Papp, S., 1998. Isotope hydrogeological study of the thermal karst system in the Buda Mountains, Hungary. RMZ-Mater. Geoenviron. 45 (1–2), 8–12.

Bada, G., Fodor, L., Székely, B., Timár, G., 1996. Tertiary brittle faulting and stress field evolution in the Gerecse Mts., N. Hungary. Tectonophysics 255, 269–289.

Bakacsi, Zs, Mindszenty, A., 2004. Pleistocene Travertine Deposits of Süttő (Gerecse Hills, Hungary). Excursion Guide, Climate and Tectonic Controls on Travertine Formation: The Case of the Pannonian Basin. Field Course, Tata, Egerszalók. pp. 13–20.

Bargar, K.E., 1978. Geology and thermal history of Mammoth Hot springs, Yellowstone National Park, Wyoming. U.S. Geol. Surv. Bull. 1444, 1–55.

Berardi, G., Vignaroli, G., Billi, A., Rossetti, F., Soligo, M., Kele, S., Baykara, M.O., Bernasconi, S.M., Castorina, F., Tecce, F., Shen, C.-C., 2016. Growth of a Pleistocene giant carbonate vein and nearby thermogene travertine deposits at Semproniano, southern Tuscany, Italy: estimate of CO2 leakage. Tectonophysics 690, 219–239.

Bersezio, R., Mele, M., Giudici, M., 2012. Imaging of subsurface alluvial stratigraphy: an electro-stratigraphic traverse across the Po Plain in Lombardy. Rend. Online Soc. Geol. Ital. 21, 1026–1028.

Bertini, A., Minissale, A., Ricci, M., 2008. Use of Quaternary travertine of central-southern Italy as archives of paleoclimate, paleohydrology and neotectonics. Ital. J. Quatern. Sci. 21, 99–112.

Bosch, F.P., 2002. Shallow Depth Karst Structure Imaging With the Very Low Frequency-Electromagnetics-GRADIENT Method (VLF-EM-GRAD): A New Geophysical Contribution to Aquifer Protection Strategies Compared With Other Near Surface Mapping Geophysics. Ph.D. thesis. Center of Hydrogeology, University of Neuchâtel, Switzerland.

Bottinga, Y., 1968. Calculation of fractionation factors for carbon and oxygen in the system calcite–carbon dioxide–water. J. Phys. Chem. 72, 800–808.

Brand, W.A., Assonov, S.S., Coplen, T.B., 2010. Correction for the 17O interference in $\delta^{13}C$ measurements when analyzing CO_2 with stable isotope mass spectrometry (IUPAC technical report). Pure Appl. Chem. 82, 1719–1733.

Brass, G.W., 1976. The variation of the marine $^{87}Sr/^{86}Sr$ ratio during Phanerozoic time: interpretation using a flux model. Geochim. Cosmochim. Acta 40 (7), 721–730.

Brogi, A., Capezzuoli, E., 2009. Travertine deposition and faulting: the fault-related travertine fissure-ridge at Terme S. Giovanni, Rapolano Terme (Italy). E. Int. J. Earth Sci. 98 (4), 931–947.

Brogi, A., Capezzuoli, E., 2014. Earthquake impact on fissure–ridge type travertine deposition. Geol. Mag. 151 (6), 1135–1143.

Brogi, A., Capezzuoli, E., Martini, I., Picozzi, M., Sandrelli, F., 2014a. Late Quaternary tectonics in the inner Northern Apennines (Siena Basin, southern Tuscany, Italy) and their seismotectonic implication. J. Geodyn. 76, 25–45.

Brogi, A., Capezzuoli, E., Alçiçek, M.C., Gandin, A., 2014b. Evolution of a fault–controlled travertine fissure–ridge in the western Anatolia extensional province: the Çukurbağ fissure–ridge (Pamukkale, Turkey). J. Geol. Soc. Lond. 171, 425–441.

Brogi, A., Liotta, D., Ruggieri, G., Capezzuoli, E., Meccheri, M., Dini, A., 2016a. An overview on the characteristics of geothermal carbonate reservoirs in southern Tuscany. Ital. J. Geosci. 135, 17–29.

Brogi, A., Alçiçek, C., et al., 2016b. Hydrothermal fluids circulation and travertine deposition in an active tectonic setting: insights from the Kamara geothermal area (western Anatolia, Turkey). Tectonophysics 680, 211–232.

Brogi, A., Capezzuoli, E., Kele, S., Baykara, M.O., Shen, C.-C., 2017. Key travertine tectofacies for neotectonics and palaeoseismicity reconstruction: effects of hydrothermal overpressured fluid injection. J. Geol. Soc. https://doi.org/10.1144/jgs2016–124.

Burgener, L., Huntington, K.W., Hoke, G.D., Schauer, A., Ringham, M.C., Latorre, C., Díaz, F., 2016. Variations in soil carbonate formation and seasonal bias over >4 km of relief in the western Andes (30°S) revealed by clumped isotope thermometry. Earth Planet. Sci. Lett. 441, 188–199.

Caine, S.J., Evans, J.P., Forster, C.B., 1996. Fault zone architecture and permeability structure. Geology 24, 1025–1028.

Capezzuoli, E., Gandin, A., Pedley, M., 2014. Decoding tufa and travertine (fresh water carbonates) in the sedimentary record: the state of the art. Sedimentology 61, 1–21.

Capezzuoli, E., Ruggieri, G., Rimondi, V., Brogi, A., Liotta, D., Alçiçek, M.C., Alçiçek, H., Bülbül, A., Gandin, A., Meccheri, M., Shen, C.C., Baykara, M.O., 2018. Calcite veining and feeding conduits in a hydrothermal system: insights from a natural section across the Pleistocene Gölemezli travertine depositional system (western Anatolia, Turkey). Sediment. Geol. 364, 180–203. https://doi.org/10.1016/j.sedgeo.2017.12.012.

Chafetz, H.S., Folk, R.L., 1984. Travertines: depositional morphology and the bacterially-constructed constituents. J. Sediment. Petrol. 54, 289–316.

Cheng, H., Edwards, R.L., Shen, C.C., Polyak, V.J., Asmerom, Y., Woodhead, J., Hellstrom, J., Wang, Y., Kong, X., Spötl, C., Wang, X., 2013. Improvements in ^{230}Th dating, ^{230}Th and ^{234}U half-life values, and U–Th isotopic measurements by multi-collector inductively coupled plasma mass spectrometry. Earth Planet. Sci. Lett. 371, 82–91.

Choquette, P.W., Pray, L.C., 1970. Geologic nomenclature and classification of porosity in sedimentary carbonates. AAPG Bull. 54 (2), 207–250.

Claes, H., Soete, J., Van Noten, K., El Desouky, H., Erthal, M.M., Vanhaecke, F., Özkul, M., Swennen, R., 2015. Sedimentology, three-dimensional geobody reconstruction and carbon dioxide origin of Pleistocene travertine deposits in the Ballık area (southwest Turkey). Sedimentology 62 (5), 1408–1445.

Claes, H., Degros, M., Soete, J., Claes, S., Kele, S., Mindszenty, A., Török, Á., El Desouky, H., Vanhaecke, G., Swennen, R., 2017. Geobody architecture, genesis and petrophysical characteristics of the Budakalász travertines, Buda Hills (Hungary). Quat. Int. Special Volume 437, 107–128.

Claes, H., Huysmans, M., Soete, J., Dirix, K., Vassilieva, E., Marques Erthal, M., Vandewijngaerde, W., Hamaekers, H., Aratman, C., Özkul, M., Swennen, R., 2019. Elemental geochemistry to complement stable isotope data of fossil travertine: importance of digestion method and statistics. Sediment. Geol. 386, 118–131.

Clark, I.D., Khoury, H.N., Salameh, E., Fritz, P., Goksu, Y., Wiesser, A., Fontes, J.-C., Causse, C., 1991. Travertines in central Jordan: implications for palaeohydrology and dating. Isotope Techniques in Water Resources Development. IAEA, Vienna, pp. 551–566.

Coplen, T.B., 2007. Calibration of the calcite-water oxygen-isotope geothermometer at Devils Hole, Nevada, a natural laboratory. Geochim. Cosmochim. Acta 71, 3948–3957.

Crossey, L.J., Fischer, T.P., Patchett, J.P., Karlstrom, K.E., Hilton, D.R., Newell, D.L., Hunton, P., Reynolds, A.C., de Leeuw, G.A.M., 2006. Dissected hydrologic system at the Grand Canyon: interaction between deeply derived fluids and plateau aquifer waters in modern springs and travertine. Geology 34 (1), 25–28.

Csillag, G., Fodor L., Ruszkiczay-Rüdiger Zs., Lantos Z., Thamóné Bozsó E., Babinszki E., Szappanos B., Kaiser M. (2018). Fluvial, fluvial-proluvial, proluvial formations. In Budai T. (ed) Geology of the Gerecse Hills. Explanatory book to the geological map of the Gerecse Hills. Published by the Hungarian Mining and Geological Survey.

Curewitz, D., Karson, J.A., 1997. Structural settings of hydrothermal outflow: fracture permeability maintained by fault propagation and interaction. J. Volcanol. Geotherm. Res. 79, 149–168.

D'Argenio, B., Ferreri, V., 1987. A brief outline of sedimentary models for Pleistocene travertine accumulation in Southern Italy. Rend. Soc. Geol. Ital. 9, 167–170.

De Boever, E., Brasier, A.T., Foubert, A., Kele, S., 2017. What do we really know about early diagenesis of non-marine carbonates? Sediment. Geol. 361, 25–51.

Deines, P., Langmuir, D., Harmon, R.S., 1974. Stable carbon isotope ratios and the existence of a gas phase in the evolution of carbonate groundwaters. Geochim. Cosmochim. Acta 38, 1147–1164.

Della Porta, G., 2015. Carbonate build-ups in lacustrine, hydrothermal and fluvial settings: comparing depositional geometry, fabric types and geochemical signature. Microbial Carbonates in Space and Time: Implications for Global Exploration and Production. Geological Society, London, Special Publications 418.

Dennis, K.J., Affek, H.P., Passey, B.H., Schrag, D.P., Eiler, J.M., 2011. Defining an absolute reference frame for 'clumped' isotope studies of CO2. Geochim. Cosmochim. Acta 75 (22), 7117–7131.

Dunham, R.J., 1962. Classification of carbonate rocks according to depositional texture. In: Ham, W.E. (Ed.), Classification of Carbonate Rocks. AAPG Memoir, Tulsa, Oklahoma, pp. 108–120.

Fischer, G., Schnegg, P.A., Peguiron, M., Lequang, B.V., 1981. An analytic one-dimensional magnetotelluric inversion scheme. Geophys. J. R. Astron. Soc. 67, 257–278.

Fodor, L. and Lantos, Z., 1998. Liassic brittle structures in the Gerecse (in Hungarian). Bulletin of the Hungarian Geol. Soc. 128/2–3, 375–396.

Fodor, L., Csontos, L., Bada, G., Györfi, I., Benkovics, L., 1999. Tertiary tectonic evolution of the Pannonian basin system and neighboring orogens: a new synthesis of paleostress data. In: Durand, B., Jolivet, L., Horváth, F., Séranne, M. (Eds.), The Mediterranean Basins: Tertiary Extension Within the Alpine Orogen. Geological Society, London, pp. 295–334.

Fodor, L., Sztanó, O., Kövér, Sz, 2013. Pre-conference field trip: Mesozoic deformation of the northern Transdanubian Range (Gerecse and Vértes Hills). Acta Miner. Petrogr. Field Guide Ser. 31, 1–34.

Fodor, L., Kercsmár, Zs, Kövér, Sz, 2018. Structural geology. In: Budai, T. (Ed.), Geology of the Gerecse Mts. Mining and Geological Survey of Hungary, Budapest. ISBN: 978-963-671-312-6, pp. 167–205.

Folk, R.L., 1959. Practical petrographic classification of limestones. AAPG Bulletin 43. Oklahoma, Tulsa.

Frery, E., Gratier, J.-.P., Ellouz–Zimmerman, N., Deschamps, P., Blamart, D., Hamelin, B., Swennen, R., 2016. Geochemical transect through a travertine mount: a detailed record of CO2–enriched fluid leakage from Late Pleistocene to present–day e Little Grand Wash fault (Utah, USA). Quat. Int. 437, 98–106.

Friedman, I. and O'Neil, J.R., 1977. Chapter KK. Compilation of stable isotope fractionation factors of geochemical interest. In Data of Geochemistry, Sixth Edition, Geological Survey Professional Paper 440.

Gandin, A., Capezzuoli, E., 2014. Travertine: distinctive depositional fabrics of carbonates from thermal spring systems. Sedimentology 61, 264–290.

Geurts, M.-A., Frappier, M., Tsien, H.H., 1992. Morphogenèse des barrages de travertin de Coal River Springs, Sud-est du territoire du Yukon. Géog. Phys. Quatern. 46, 221–232.

Gradziński, M., Wróblewski, W., Duliński, M., Hercman, H., 2014. Earthquake-affected development of a travertine ridge. Sedimentology 61, 238–263. https://doi.org/10.1111/sed.12086.

Guo, L., Riding, R., 1992. Micritic aragonite laminae in hot water travertine crust, Rapolano Terme. Sedimentology 39, 1067–1079.

Guo, L., Riding, R., 1994. Origin and diagenesis of Quaternary travertine shrub fabrics, Rapolano Terme, Central Italy. Sedimentology 41, 499–520.

Guo, L., Riding, R., 1998. Hot–spring travertine facies and sequences, late Pleistocene, Rapolano Terme, Italy. Sedimentology 45, 163–180.

Haas, J., 2001. Geology of Hungary. Eötvös University press, p. 317.

Hancock, P.L., Chalmers, R.M.L., Altunel, E., Çakir, Z., 1999. Travitonics: using travertines in active fault studies. J. Struct. Geol. 21, 903–916.

He, B., Olack, G.A., Colman, A.S., 2012. Pressure baseline correction and high-precision CO_2 clumped isotope (Δ47) measurements in bellows and micro-volume modes. Rapid Commun. Mass Spectrom. 26, 2837–2853.

Hoefs, J., 2009. Stable Isotope Geochemistry. Springer-Verlag, Berlin 285 p.

Horváth, F., 1993. Towards a mechanical model for the formation of the Pannonian basin. Tectonophysics 226, 333–357.

Horváth, F., Cloetingh, S., 1996. Stress-induced late stage subsidence anomalies in the Pannonian basin. Tectonophysics 266, 287–300.

Inoue, H., Sugimura, Y., 1985. Carbon isotopic fractionation during the CO2 exchange process between air and sea water under equilibrium and kinetic conditions. Geochimica et Cosmochimica Acta, 49. Issue 11, 2453–2460.

Jeandel, E., Battani, A., Sarda, P., 2010. Lessons from natural and industrial analogues for storage of carbon dioxide. Int. J. Greenhouse Gas Control 4, 890–909.

Kele, S., 2009. Investigations on Freshwater Limestones From the Carpathian-Basin: Palaeoclimatological and Sedimentological Studies. PhD thesis. Eötvös Loránd University, Budapest (Hungary) 176 p.

Kele, S., Demény, A., Siklósy, Z., Németh, T., Mária, T., B.Kovács, M., 2008. Chemical and stable isotope compositions of recent hot-water travertines and associated thermal waters, from Egerszalók, Hungary: depositional facies and non-equilibrium fractionations. Sediment. Geol. 211, 53–72.

Kele, S., Özkul, M., Fórizs, I., Gökgöz, A., Baykara, M.O., Alçiçek, M.C., 2011. Stable isotope geochemical study of Pamukkale travertines: new evidences of low-temperature non-equilibrium calcite-water fractionation. Sediment. Geol. 238, 191–212.

Kele, S., Breitenbach, S.F.M., Capezzuoli, E., Meckler, A.N., Ziegler, M., Millan, I.M., Kluge, T., Deák, J., Hanselmann, K., John, C.M., Yan, H., Liu, Z., Bernasconi, S.M., 2015. Temperature dependence of oxygen- and clumped isotope fractionation in carbonates: a study of travertines and tufas in the 6–95 °C temperature range. Geochim. Cosmochim. Acta 168, 172–192.

Kelson, J.R., Huntington, K.W., Schauer, A.J., Saenger, C., Lechler, A.R., 2017. Toward a universal carbonate clumped isotope calibration: diverse synthesis and preparatory methods suggest a single temperature relationship. Geochim. Cosmochim. Acta 197, 104–131.

Kim, S.-T., O'Neil, J.R., 1997. Equilibrium and nonequilibrium oxygen isotope effects in synthetic carbonates. Geochim. Cosmochim. Acta 61, 3461–3475.

Krzywinski, M., Almtan, N., 2014. Visualizing samples with box plots. Nat. Methods 11, 119–120.

Lantos, M., 2004. Magnetostratigraphic correlation of Quaternary travertine sequences in NE Transdanubia. Bulletin of the Hungarian Geol. Soc. 134 (2), 227–236.

Leng, M.J., Marshall, J.D., 2004. Paleoclimate interpretation of stable isotope data from lake sediment archives. Quat. Sci. Rev. 23, 811–831.

Livnat, A., Kronfeld, J., 1985. Paleoclimatic implications of U-series dates for lake sediments and travertines in the Arava Rift Valley. Israel. Quat. Res. 24, 164–172.

Loke, M.H., Chambers, J.E., Rucker, D.F., Kuras, O., Wilkinson, P.B., 2013. Recent developments in the direct-current geoelectrical imaging method. J. Appl. Geophys. 95, 135–156.

Mádl-Szőnyi, J., Tóth, Á., 2015. Basin-scale conceptual groundwater flow model for an unconfined and confined thick carbonate region. Hydrogeol. J. 23, 1359–1380.

McArthur, M.J., Howarth, R.J., Bailey, T.R., 2001. Strontium isotope stratigraphy: LOWESS version 3: best fit to the marine Sr-isotope curve for 0–509 Ma and accompanying look-up table for deriving numerical age. J. Geol. 109 (2), 155–170.

Mele, M., Bersezi, R., Giudici, M., 2012. Hydrogeophysical imaging of alluvial aquifers: electrostratigraphic unit sin the quaternary Po alluvial plain (Italy). Int. J. Earth Sci. (Geol. Rundsch.) 101, 2005–2025.

Minissale, A., 2004. Origin, transport and discharge of CO2 in central Italy. Earth-Science Reviews Volume 66. Issues 1–2, 89–141.

Minissale, A., Kerrick, D.M., Magro, G., Murrell, M.T., Paladini, M., Rihs, S., Sturchio, N.C., Tassi, F., Vaselli, O., 2002. Geochemistry of Quaternary travertines in the region north of Rome (Italy): structural, hydrologic and paleoclimatic implications. Earth Planet. Sci. Lett. 203, 709–728.

Mohammadi, Z., Capezzuoli, E., Claes, H., Alipoor, R., Muchez, P., Swennen, R., 2019. Substrate geology controlling different morphology, sedimentology, diagenesis and geochemistry of adjacent travertine bodies: a case study from the Sanandaj-Sirjan zone (western Iran). Sediment. Geol. 389, 127–146.

Novothny, Á., Frechen, M., Horváth, E., Wacha, L., Rolf, C., 2011. Investigating the penultimate and last glacial cycles of the Süttö loess section (Hungary) using luminescence dating, high-resolution grain size, and magnetic susceptibility data. Quat. Int. 234, 75–85.

Palacky, G.J., 1988. Resistivity characteristics of geologic targets. SEG 1, 53–129.

Panichi, C., Tongiorgi E. 1976. Carbon isotopic composition of CO2 from springs, fumaroles, mofettes and travertines of central and southern Italy: a preliminary prospection method of geothermal areas. – Proc. 2nd U. N. Symp. on the Develop. and Use of Geotherm. Energy, San Francisco, 20–29 May 1975, 815–825.

Pazonyi, P., Kordos, L., Magyari, E., Marinova, E., Füköh, L., Venczel, M., 2014. Pleistocene vertebrate faunas of the Süttő Travertine Complex (Hungary). Quat. Int. 319, 50–63.

Pécsi, M., 1959. Formation and geomorphology of the Danube valley in Hungary. Akadémiai kiadó 346, Budapest.

Pécsi, M., 1970. Geomorphological Regions of Hungary. Geographical Research Institute, Hungarian Academy of Science, Budapest.

Pedley, H.M., 1990. Classification and environmental models of cool freshwater tufas. Sediment. Geol. 68, 143–154.

Pentecost, A., 2005. Travertine. Springer-Verlag, Berlin.

Pola, M., Gandin, A., Tuccimei, P., Soligo, M., Deiana, R., Fabbri, P., Zampieri, D., 2014. A multidisciplinary approach to understanding carbonate deposition under tectonically controlled hydrothermal circulation: a case study from a recent travertine mound in the Euganean hydrothermal system, northern Italy. Sedimentology 61, 172–199.

Richards, D.A., Dorale, J.A., 2003. Uranium-series chronology and environmental applications of speleothems. Rev. Mineral. Geochem. 52 (1), 407–460.

Rolf, C., Hambach, U., Novothny, Á., Horváth, E., Schnepp, E., 2014. Dating of a Last Glacial loess sequence by relative geomagnetic palaeointensity: a case study from the Middle Danube Basin (Süttő, Hungary). Quat. Int. 319, 99–108.

Rollinson, H.R., 1993. Using Geochemical Data: Evaluation, Presentation. Interpretation, Longman Geochemistry Series, Longman Group UK Limited, Pearson Education Limited.

Ronchi, P., Cruciani, F., 2015. Continental carbonates as a hydrocarbon reservoir, an analog case study from the travertine of Saturnia, Italy. AAPG Bull. 99 (4), 711–734. https://doi.org/10.1306/10021414026.

Rose, T.P., Davisson, M.L., 1996. Radiocarbon in hydrologic systems containing dissolved magmatic carbon dioxide. Science 273, 1367–1370.

Royden, L.H., Horváth, F., 1988. The Pannonian basin - A study in basin evolution. AAPG Mem. 45, 49–55 Tulsa.

Ruszkiczay-Rüdiger, Zs, Fodor, L., Bada, G., Leél-Őssy, Sz, Horváth, E., Dunai, T.J., 2005. Quantification of Quaternary vertical movements in the central Pannonian Basin: a review of chronologic data along the Danube river, Hungary. Tectonophysics 410, 157–172.

Ruszkiczay-Rüdiger, Zs, Fodor, L., Csillag, G., Braucher, R., Kele, S., Novothny, Á., Thamó-Bozsó, E., Virág, A., Molnár, G., Madarász, B., ASTER Team, 2016. Spatially and temporally varying Quaternary uplift rates of the Gerecse Hills, Northern Pannonian Basin, using dated geomorphological horizons in the Danube valley. Geophysical Research Abstracts 18, EGU2016-6463. Quat. Sci. Rev. 131, 127–147.

Ruszkiczay-Rüdiger, Zs, Csillag, G., Fodor, L., Braucher, R., Novothny, Á., Thamó-Bozsó, E., Virág, A., Pazonyi, P., Timár, G., Team, A.S.T.E.R., 2018. Integration of new and revised chronological data to constrain the terrace evolution of 1 the Danube River (Gerecse Hills, Pannonian Basin). Quat. Geochronol. 48, 148–170. https://doi.org/10.1016/j.quageo.2018.08.003.

Sano, Y., Marty, B., 1995. Origin of carbon in fumarolic gas from island arcs. Chem. Geol. 119, 265–274.

Schauer, A.J., Kelson, J., Saenger, C., Huntington, K.W., 2016. Choice of 17O correction affects clumped isotope (Δ47) values of CO_2 measured with mass spectrometry. Rapid Commun. Mass Spectrom. 30, 2607–2616.

Scheuer, G., Schweitzer, F., 1988. A Gerecse és a Budai-hegység édesvízi mészkőösszletei. Földrajzi Tanulmányok 20. Akadémiai Kiadó, Budapest, p. 131.

Sharp, Z.D., Papike, J.J., Durakiewicz, T., 2003. The effect of thermal decarbonation on stable isotope compositions of carbonates. Am. Mineral. 88, 87–92.

Shen, C.-C., Edwards, R.L., Cheng, H., Dorale, J.A., Thomas, R.B., Moran, S.B., Weinstein, S.E., Edmonds, H.N., 2002. Uranium and thorium isotopic and concentration measurements by magnetic sector inductively coupled plasma mass spectrometry. Chem. Geol. 185, 165–178.

Shen, C.-C., Wu, C.-C., Cheng, H., Edwards, R.L., Hsieh, Y.-T., Gallet, I., Chang, C.-C., Li, T.-Y., Lam, D.D., Kano, A., Hori, M., Spötl, C., 2012. High-precision and high-resolution carbonate 230Th dating by MC-ICP-MS with SEM protocols. Geochim. Cosmochim. Acta 99, 71–86.

Sierralta, M., Kele, S., Melcher, F., Hambach, U., Reinders, J., van Geldern, R., Frechen, M., 2010. Characterization and uranium-series dating of travertine from Süttő in Hungary. Quat. Int. 222, 178–193.
Snoeck, C., Lee-Thorp, J., Schulting, R., de Jong, J., Debouge, W., Mattielli, N., 2015. Calcined bone provides a reliable substrate for strontium isotope ratios as shown by an enrichment experiment. Rapid Commun. Mass Spectrom. 29 (1), 107–114.
Soete, J., Kleipool, L.M., Claes, H., Claes, S., Hamaekers, H., Kele, S., Özkul, M., Foubert, A., Reijmer, J.J.G., Swennen, R., 2015. Acoustic properties in travertines and their relation to porosity and pore types. Mar. Pet. Geol. 320–335.
Spötl, C., Vennemann, T.W., 2003. Continuous-flow isotope ratio mass spectrometric analysis of carbonate minerals. Rapid Commun. Mass Spectrom. 17, 1004–1006.
Teboul, P.-A., Durlet, C., Gaucher, E.C., Virgone, A., Girard, J.-P., Curie, J., Lopez, B., Camoin, G.F., 2016. Origins of elements building travertine and tufa: new perspectives provided by isotopic and geochemical tracers. Sediment. Geol. 334, 97–114.
Török, Á., 2018. The Anatomy of a Pleistocene Travertine Complex – Sedimentological, Diagenetic and Reservoir Studies on the Süttő Travertine System (Gerecse Hills, Hungary). PhD Thesis. Eötvös Loránd University (Hungary) and Katholieke Universiteit Leuven (Belgium), p. 150.
Török, Á., Mindszenty, A., Claes, H., Kele, S., Fodor, L., Swennen, R., 2017. Geobody architecture of continental carbonates: "Gazda" travertine quarry (Süttő, Gerecse Hills, Hungary). Quat. Int. 437, 164–185.
Turberg, P.I., Müller, I., Flury, F., 1994. Hydrogeological investigation of porous environments by radiomagnetotelluric resistivity (RMT-R 12-240 kHz). J. Appl. Geophys. 31, 133–143.
Uysal, T., Feng, Y., Zhao, J., Altunel, E., Weatherley, D., Karabacak, V., Cengiz, O., Golding, S.D., Lawrence, M.G., Collerson, K.D., 2007. U-series dating and geochemical tracing of late Quaternary travertines in coseismic fissures. Earth Planet. Sci. Lett. 257, 450–462.
Uysal, I.T., Feng, Y., Zhao, J., Isik, V., Nuriel, P., Golding, S., 2009. Hydrothermal CO2 degassing in seismically active zones during the late Quaternary. Chem. Geol. 265, 442–454.
Van Noten, K., Claes, H., Soete, J., Foubert, A., Özkul, M., Swennen, R., 2013. Fracture networks and strike – slip deformation along reactivated normal faults in Quaternary travertine deposits, Denizli Basin, western Turkey. Tectonophysics 588, 154–170.
Véghné, S., Kriván, P., Gyóvai, L., Mészáros, I., 1971. A Süttői (Komárom megye) díszítőkő kutatás összefoglaló földtani jelentése és készletszámítása. MÁFI Report from 1971, 188.
Vignaroli, G., Berardi, G., Billi, A., Kele, S., Rossetti, F., Soligo, M., Bernasconi, S.M., 2016. Tectonics, hydrothermalism, and paleoclimate recorded by Quaternary travertines and their spatio-temporal distribution in the Albegna basin, central Italy: insights on Tyrrhenian margin neotectonics. Lithosphere 8, 335–358.
Wéber, Z., 2016. Probabilistic waveform inversion for 22 earthquake moment tensors in Hungary: new constraints on the tectonic stress pattern inside the Pannonian basin. Geophys. J. Int. 204, 236–249.
Wéber, Z., Süle, B., 2014. Source properties of the 29 January 2011 ML 4.5 Oroszlány (Hungary) mainshock and its aftershocks. Bull. Seismol. Soc. Am. 104 (1), 113–1127.
Weis, D., Kieffer, B., Maerschalk, C., Barling, J., de Long, J., Williams, G.A., Hanano, D., Pretorius, W., Mattielli, N., Scoate, J.S., Goolaerts, A., Friedman, R.M., Mahoney, J.B., 2006. High-precision isotopic characterization of USGS reference materials by TIMS and MC-ICP-MS. Geochem. Geophys. Geosyst. 7 (8), 1–30.
Woodhead, J., Hellstrom, J., Maas, R., Drysdale, R., Zanchetta, G., Devine, P., Taylor, E., 2006. U-Pb geochronology of speleothems by MC-ICPMS. Quat. Geochronol. 1, 208–221.
Yan, H., Sun, H., Liu, Z., 2012. Equilibrium vs. kinetic fractionation of oxygen isotopes in two low-temperature travertine-depositing systems with differing hydrodynamic conditions at Baishuitai, Yunnan, SW China. Geochim. Cosmochim. Acta 95, 63–78.